

# MONKES: a fast neoclassical code for the evaluation of monoenergetic transport coefficients

F. J. Escoto<sup>1</sup>, J. L. Velasco<sup>1</sup>, I. Calvo<sup>1</sup>, M. Landreman<sup>2</sup> and F. I. Parra<sup>3</sup>

<sup>1</sup>Laboratorio Nacional de Fusión, CIEMAT, 28040 Madrid, Spain

<sup>2</sup>University of Maryland, College Park, MD 20742, USA

<sup>3</sup>Princeton Plasma Physics Laboratory, Princeton, NJ 08540, USA

E-mail: [fjavier.escoto@ciemat.es](mailto:fjavier.escoto@ciemat.es)

April 2023

**Abstract.** MONKES is a new neoclassical code for the evaluation of monoenergetic transport coefficients in large aspect ratio stellarators. By means of a convergence study and benchmarks with other codes, it is shown that MONKES is accurate and efficient. The combination of spectral discretization in spatial and velocity coordinates with block sparsity allows MONKES to compute monoenergetic coefficients at low collisionality, in a single processor, in approximately one minute. MONKES is sufficiently fast to be integrated into stellarator optimization codes for direct optimization of the bootstrap current and to be included in predictive transport suites.

*Keywords:* stellarator optimization, neoclassical transport, bootstrap current.  
Submitted to: *Nucl. Fusion*

## 1. Introduction

Stellarators are an attractive alternative to tokamaks as future fusion reactors. While tokamaks require a large toroidal current to generate part of the magnetic field, in stellarators the field is produced entirely by external magnets. As a consequence, stellarators avoid current-induced instabilities and facilitate the steady-state operation. These advantages come at the expense of making the magnetic field three-dimensional. In tokamaks, axisymmetry guarantees that the radial displacement that charged particles experience along their collisionless orbits averages to zero. Therefore, in the absence of collisions, all charged particles are confined. However, in a generic stellarator the orbit-averaged radial drift velocity does not vanish for trapped particles and they quickly drift out of the device. The combination of a non zero orbit-averaged radial drift and a small collision frequency (reactor-relevant fusion plasmas are weakly collisional in the core) produces, for a generic stellarator, intolerably large levels of neoclassical transport.

Hence, stellarator magnetic fields must be carefully designed in order to display good confinement properties. This process of tailoring of the magnetic field is called stellarator optimization. The goal of neoclassical optimization is to obtain a stellarator with levels of neoclassical losses equivalent or lower to those in an axisymmetric device. Stellarator magnetic fields in which the orbit-averaged radial magnetic drift is zero for all particles are called omnigenous [1]. Thus, the goal of neoclassical optimization is to obtain magnetic fields which are close to omnigenicity. However, addressing only radial transport in the optimization process is not sufficient. In toroidal plasmas, the parallel flow of electrons and the rest of species is not, in general, balanced. This mismatch produces a net parallel current at each flux surface which, through Ampère's law, modifies the magnetic field  $\mathbf{B}$ . When the current is generated by neoclassical mechanisms and non-zero plasma profile gradients, we speak of bootstrap current. The bootstrap current and its effect on the magnetic configuration must be taken into account in the design of optimized stellarator magnetic fields.

Two different subclasses of omnigenous stellarators have drawn particular attention: quasi-isodynamic (QI) and quasi-symmetric (QS) stellarators. Quasi-isodynamic configurations are omnigenous configurations in which the curves of constant magnetic field strength  $B := |\mathbf{B}|$  on a flux surface close poloidally. This additional property has an important implication: QI stellarators produce zero bootstrap current at low collisionality [2, 3]. Thanks to this feature, QI stellarators can control plasma-wall interaction by means of a divertor relying on a specific structure of islands, which cannot be realized in the presence of large toroidal cur-

rents. The Wendelstein 7-X (W7-X) experiment was designed to be close to QI and demonstrates that theoretically based stellarator optimization can be applied to construct a device with much better confinement properties than any previous stellarator [4]. Despite its success, there is still room for improvement. The two principal configurations of W7-X, the KJM or so-called “high mirror” and the EIM also known as “standard” are not optimized for simultaneously having low levels of radial and parallel transport [5]. Consequently, optimization of QI stellarators is a very active branch of research and enormous effort has been put in pushing forward the design and construction of quasi-isodynamic stellarators [6, 7, 8, 9, 10].

The QS subclass of omnigenous configurations is attractive as the neoclassical properties of such magnetic fields are isomorphic to those in a tokamak [11, 12]. It has been shown that it is possible to design QS magnetic fields with extremely low neoclassical losses [13]. In contrast to QI configurations, QS stellarators are expected to have a substantial bootstrap current<sup>‡</sup>. Examples of this subclass are the Helically Symmetric eXperiment (HSX) [15] or the design National Compact Stellarator Experiment (NCSX) [16].

At each iteration of the optimization process it is necessary to evaluate a large number ( $\sim 10^2$ ) of magnetic configurations. Therefore, in order to neoclassically optimize a magnetic field it is required to be able to evaluate fast the neoclassical properties of each configuration. Due to this requirement, neoclassical properties are typically addressed indirectly. One example of addressing indirectly neoclassical properties comes from knowing that in an omnigenous stellarator local maxima and minima of  $B$  along field lines are aligned. Therefore, it seems reasonable to try to align these extrema in neoclassical optimization. Another example is to optimize pursuing that the isolines of  $B$  close poloidally on a flux surface, hoping to achieve quasi-isodynamicity. A different manner to address indirectly neoclassical properties is through figures of merit for the collisional regime of interest. For the  $1/\nu$  regime, the code NEO [17] computes the effective ripple  $\epsilon_{\text{eff}}$ , which encapsulates the dependence on the magnetic configuration of radial neoclassical transport. For transport within the flux surface, there exist long mean free path formulae for parallel flow and bootstrap current [18, 19, 20]. Although they can be computed very fast and might capture some qualitative behaviour, these formulae are plagued with noise due to resonances in rational surfaces and, even with

<sup>‡</sup> With the exception of the quasi-poloidally symmetric magnetic field, which lies at the intersection of QI and QS configurations. However, quasi-poloidal symmetry is impossible to achieve near the magnetic axis [14].

smoothing ad-hoc techniques, they are not accurate [21]. This lack of accuracy limits their application for optimization purposes. During the optimization process, an accurate calculation of the bootstrap current is required to account for its effect (e.g. for optimizing QS stellarators) or to keep it sufficiently small (when optimizing for quasi-isodinamicity).

Recent developments allow direct optimization of radial neoclassical transport. Based on rigorous derivations [22, 23], the code KNOSOS [24, 25] solves very fast an orbit-averaged drift-kinetic equation that is accurate for low collisionality regimes. KNOSOS is included in the stellarator optimization suite STELOPT [26].

In this work we present MONKES (MONoenergetic Kinetic Equation Solver), a new neoclassical code conceived to satisfy the necessity of fast and accurate calculations of the bootstrap current for stellarator optimization. Specifically, MONKES makes it possible to include among the optimization targets the monoenergetic coefficients  $\hat{D}_{ij}$  where  $i, j \in \{1, 2, 3\}$  (their precise definition is given in section 2). These nine coefficients encapsulate the neoclassical transport across and within flux surfaces. The coefficients  $\hat{D}_{ij}$  for  $i \in \{1, 2\}$  allow to compute the flux of particles and heat across the flux surface. For transport within the flux surface, the parallel flow of each species can be calculated in terms of the coefficients  $\hat{D}_{3j}$ . In the absence of externally applied loop voltage, the bootstrap current is driven by the radial electric field and gradients of density and temperature. The so-called bootstrap current coefficient  $\hat{D}_{31}$  is the one that relates the parallel flow to these gradients. Since MONKES computes fast the radial transport coefficients, it will also allow to optimize taking into account the  $1/\nu$  to plateau transition (something that KNOSOS, an orbit-averaged code, cannot do). Apart from optimization, MONKES can find many other applications. For instance, it can be used for the analysis of experimental discharges or also be included in predictive transport frameworks such as TANGO [27] and TRINITY [28].

This paper is organized as follows: in section 2, we introduce the drift-kinetic equation solved by MONKES and the transport coefficients that it computes. In section 3, we explain the algorithm used to solve the drift-kinetic equation and its implementation. In section 4, by means of a convergence study, we demonstrate that MONKES can be used to compute accurate monoenergetic coefficients at low collisionality very fast for the  $1/\nu$  and  $\sqrt{\nu}$  regimes. MONKES results are also benchmarked against DKES [29] and, when necessary, against SFINCS [30]. Finally, in section 5 we summarize the results and discuss future lines of work.

## 2. Drift-kinetic equation and transport coefficients

MONKES solves the drift-kinetic equation

$$(v\xi\mathbf{b} + \mathbf{v}_E) \cdot \nabla h_a + v \nabla \cdot \mathbf{b} \frac{(1 - \xi^2)}{2} \frac{\partial h_a}{\partial \xi} - \nu^a \mathcal{L} h_a = S_a, \quad (1)$$

where  $\mathbf{b} := \mathbf{B}/B$  is the unitary vector tangent to magnetic field lines and we have employed as velocity coordinates the cosine of the pitch-angle  $\xi := \mathbf{v} \cdot \mathbf{b}/|\mathbf{v}|$  and the magnitude of the velocity  $v := |\mathbf{v}|$ .

We assume that the magnetic configuration has nested flux surfaces. We denote by  $\psi \in [0, \psi_{\text{lcf}}]$  a radial coordinate that labels flux surfaces, where  $\psi_{\text{lcf}}$  denotes the label of the last closed flux surface. In equation (1),  $h_a$  is the non-adiabatic component of the deviation of the distribution function from a local Maxwellian for a plasma species  $a$

$$f_{Ma}(\psi, v) := n_a(\psi) \pi^{-3/2} v_{ta}^{-3}(\psi) \exp\left(-\frac{v^2}{v_{ta}^2(\psi)}\right). \quad (2)$$

Here,  $n_a$  is the density of species  $a$ ,  $v_{ta} := \sqrt{2T_a/m_a}$  is its thermal velocity,  $T_a$  its temperature (in energy units) and  $m_a$  its mass.

For the convective term in equation (1)

$$\mathbf{v}_E := \frac{\mathbf{E}_0 \times \mathbf{B}}{\langle B^2 \rangle} = -E_\psi(\psi) \frac{\mathbf{B} \times \nabla \psi}{\langle B^2 \rangle} \quad (3)$$

denotes the incompressible  $\mathbf{E} \times \mathbf{B}$  drift approximation and  $\mathbf{E}_0 = E_\psi(\psi) \nabla \psi$  is the electrostatic piece of the electric field  $\mathbf{E}$  perpendicular to the flux surface. The symbol  $\langle \dots \rangle$  stands for the flux surface average operation. Denoting by  $V(\psi)$  to the volume enclosed by the flux surface labelled by  $\psi$ , the flux surface average of a function  $f$  can be defined as the limit

$$\langle f \rangle := \lim_{\delta\psi \rightarrow 0} \frac{\int_{V(\psi+\delta\psi)} f d^3\mathbf{r} - \int_{V(\psi)} f d^3\mathbf{r}}{V(\psi+\delta\psi) - V(\psi)}, \quad (4)$$

where  $d^3\mathbf{r}$  is the spatial volume form.

We denote the Lorentz pitch-angle scattering operator by  $\mathcal{L}$ , which in coordinates  $(\xi, v)$  takes the form

$$\mathcal{L} = \frac{1}{2} \frac{\partial}{\partial \xi} \left( (1 - \xi^2) \frac{\partial}{\partial \xi} \right). \quad (5)$$

In the collision operator,  $\nu^a(v) = \sum_b \nu^{ab}(v)$  and

$$\nu^{ab}(v) := \frac{4\pi n_b e_a^2 e_b^2}{m_a^2 v_{ta}^3} \log \Lambda \frac{\text{erf}(v/v_{tb}) - G(v/v_{tb})}{v^3/v_{ta}^3} \quad (6)$$

stands for the pitch-angle collision frequency between species  $a$  and  $b$ . We denote the respective charges of

each species by  $e_a$  and  $e_b$ , the Chandrasekhar function by  $G(x) = [\text{erf}(x) - (2x/\sqrt{\pi}) \exp(-x^2)] / (2x^2)$ ,  $\text{erf}(x)$  is the error function and  $\log \Lambda$  is the Coulomb logarithm [31].

On the right-hand-side of equation (1)

$$S_a := -\mathbf{v}_{ma} \cdot \nabla \psi \left( A_{1a} + \frac{v^2}{v_{ta}^2} A_{2a} \right) f_{Ma} + Bv\xi A_{3a} f_{Ma} \quad (7)$$

is the source term,

$$\mathbf{v}_{ma} \cdot \nabla \psi = -\frac{Bv^2}{\Omega_a} \frac{1 + \xi^2}{2B^3} \mathbf{B} \times \nabla \psi \cdot \nabla B \quad (8)$$

is the expression of the radial magnetic drift assuming ideal magnetohydrodynamical equilibrium,  $\Omega_a = e_a B / m_a$  is the gyrofrequency of species  $a$ ,  $e_a$  its charge and the flux functions

$$A_{1a}(\psi) := \frac{d \ln n_a}{d\psi} - \frac{3}{2} \frac{d \ln T_a}{d\psi} - \frac{e_a E_\psi}{T_a}, \quad (9)$$

$$A_{2a}(\psi) := \frac{d \ln T_a}{d\psi}, \quad (10)$$

$$A_{3a}(\psi) := \frac{e_a}{T_a} \frac{\langle \mathbf{E} \cdot \mathbf{B} \rangle}{\langle B^2 \rangle}, \quad (11)$$

are the so-called thermodynamical forces.

Mathematically speaking, there are still two additional conditions to completely determine the problem to be solved. First, equation (1) must be solved imposing regularity conditions at  $\xi = \pm 1$

$$\left( (1 - \xi^2) \frac{\partial h_a}{\partial \xi} \right) \Big|_{\xi=\pm 1} = 0. \quad (12)$$

In second place, the solution to equation (1) is determined up to an additive function  $g(\psi, v)$ . This function is unimportant as it does not contribute to the transport coefficients. Nevertheless, in order to have a unique solution to the drift-kinetic equation, it must be fixed by imposing an appropriate additional constraint. We will select this free function (for fixed  $(\psi, v)$ ) by imposing

$$\left\langle \int_{-1}^1 h_a d\xi \right\rangle = C, \quad (13)$$

for some  $C \in \mathbb{R}$  that will be determined indirectly in section 3.

The drift-kinetic equation (1) is the one presented in [32]. An equivalent form of this equation is solved by the standard neoclassical code DKES [29] using a variational principle.

Taking the moments  $\{\mathbf{v}_{ma} \cdot \nabla \psi, (v^2/v_{ta}^2) \mathbf{v}_{ma} \cdot \nabla \psi, v\xi B\}$  of  $h_a$  and then the flux-surface average

yields, respectively, the radial particle flux, the radial heat flux and the parallel flow

$$\langle \Gamma_a \cdot \nabla \psi \rangle := \left\langle \int \mathbf{v}_{ma} \cdot \nabla \psi h_a d^3 \mathbf{v} \right\rangle, \quad (14)$$

$$\left\langle \frac{\mathbf{Q}_a \cdot \nabla \psi}{T_a} \right\rangle := \left\langle \int \frac{v^2}{v_{ta}^2} \mathbf{v}_{ma} \cdot \nabla \psi h_a d^3 \mathbf{v} \right\rangle, \quad (15)$$

$$\frac{\langle n_a \mathbf{V}_a \cdot \mathbf{B} \rangle}{B_0} := \left\langle \frac{B}{B_0} \int v\xi h_a d^3 \mathbf{v} \right\rangle, \quad (16)$$

where  $B_0(\psi)$  is a reference value for the magnetic field strength on the flux surface (its explicit definition is given in section 3).

It is a common practice for linear drift-kinetic equations (e.g. [32], [33], [30]) to apply superposition and split  $h_a$  in three additive terms. Each one of them is a solution to the drift-kinetic equation using as source one of the three summands of the right hand side of definition (7). Besides, as in the drift-kinetic equation (1) there are no derivatives or integrals along  $\psi$  nor  $v$ , it is convenient to use the splitting

$$h_a = f_{Ma} \left[ \frac{Bv}{\Omega_a} \left( A_{1a} f_1 + A_{2a} \frac{v^2}{v_{ta}^2} f_2 \right) + A_{3a} f_3 \right], \quad (17)$$

relating  $h_a$  to three functions  $\{f_j\}_{j=1}^3$ . The splitting is chosen so that the functions  $\{f_j\}_{j=1}^3$  are solutions to

$$\begin{aligned} \xi \mathbf{b} \cdot \nabla f_j + \nabla \cdot \mathbf{b} \frac{(1 - \xi^2)}{2} \frac{\partial f_j}{\partial \xi} - \frac{\hat{E}_\psi}{\langle B^2 \rangle} \mathbf{B} \times \nabla \psi \cdot \nabla f_j \\ - \hat{\nu} \mathcal{L} f_j = s_j, \end{aligned} \quad (18)$$

for  $j = 1, 2, 3$ , where  $\hat{\nu} := \nu(v)/v$  and  $\hat{E}_\psi := E_\psi/v$ . The source terms are defined as

$$s_1 := -\mathbf{v}_{ma} \cdot \nabla \psi \frac{\Omega_a}{Bv^2}, \quad s_2 := s_1, \quad s_3 := \xi \frac{B}{B_0}. \quad (19)$$

The relation between  $h_a$  and  $f_j$  given by equation (17) is such that the transport quantities (14), (15) and (16) can be written in terms of three transport coefficients which for fixed  $(\hat{\nu}, \hat{E}_\psi)$  depend only on the magnetic configuration. As  $d\hat{\nu}/dv$  never annuls, the dependence of  $f_j$  on the velocity  $v$  can be parametrized by its dependence on  $\hat{\nu}$ . Thus, for fixed  $(\hat{\nu}, \hat{E}_\psi)$ , equation (18) is completely determined by the magnetic configuration. Hence, its unique solutions  $f_j$  that satisfy conditions (12) and (13) are also completely determined by the magnetic configuration. The ad-hoc assumptions that lead to  $\psi$  and  $v$  appearing as mere parameters in the drift-kinetic equation (1) comprise the so called monoenergetic approximation to neoclassical transport (see e.g. [34]).

Using (17) we can write the transport quantities

(14), (15) and (16) in terms of the Onsager matrix

$$\begin{bmatrix} \langle \Gamma_a \cdot \nabla \psi \rangle \\ \langle \frac{\mathbf{Q}_a \cdot \nabla \psi}{T_a} \rangle \\ \langle \frac{n_a \mathbf{V}_a \cdot \mathbf{B}}{B_0} \rangle \end{bmatrix} = \begin{bmatrix} L_{11a} & L_{12a} & L_{13a} \\ L_{21a} & L_{22a} & L_{23a} \\ L_{31a} & L_{32a} & L_{33a} \end{bmatrix} \begin{bmatrix} A_{1a} \\ A_{2a} \\ A_{3a} \end{bmatrix}. \quad (20)$$

We have defined the thermal transport coefficients as

$$L_{ija} := \int_0^\infty 2\pi v^2 f_{Ma} w_i w_j D_{ija} dv, \quad (21)$$

where  $w_1 = w_3 = 1$ ,  $w_2 = v^2/v_{ta}^2$  and we have used that  $\int g d^3\mathbf{v} = 2\pi \int_0^\infty \int_{-1}^1 g v^2 d\xi dv$  for any integrable function  $g(\xi, v)$ . The quantities  $D_{ija}$  are the monoenergetic transport coefficients, defined as

$$D_{ija} := \frac{B^2 v^3}{\Omega_a^2} \hat{D}_{ij}, \quad i, j \in \{1, 2\}, \quad (22)$$

$$D_{i3a} := \frac{B v^2}{\Omega_a} \hat{D}_{i3}, \quad i \in \{1, 2\}, \quad (23)$$

$$D_{3ja} := \frac{B v^2}{\Omega_a} \hat{D}_{3j}, \quad j \in \{1, 2\}, \quad (24)$$

$$D_{33a} := v \hat{D}_{33}, \quad (25)$$

and  $\hat{D}_{ij}$  are the monoenergetic geometric coefficients

$$\hat{D}_{ij}(\psi, v) := \left\langle \int_{-1}^1 s_i f_j d\xi \right\rangle, \quad i, j \in \{1, 2, 3\}. \quad (26)$$

Note that, unlike  $D_{ija}$ , the monoenergetic geometric coefficients  $\hat{D}_{ij}$  do not depend on the species for fixed  $\hat{v}$  (however the correspondent value of  $v$  associated to each  $\hat{v}$  varies between species) and depend only on the magnetic geometry. Of the monoenergetic geometric coefficients  $\hat{D}_{ij}$  only three of them are independent as Onsager symmetry implies  $\hat{D}_{13} = -\hat{D}_{31}$ . Hence, obtaining the transport coefficients for all species requires to solve (18) for two different source terms  $s_1$  and  $s_3$ . The algorithm for solving equation (18) is described in the next section.

### 3. Numerical method

In this section we describe the algorithm implemented to numerically solve the drift-kinetic equation (18). We drop the subscript  $j$  from that labels every different source term. Also, as  $\psi$  and  $v$  act as mere parameters we will omit their dependence in this section and functions of these two variables will be referred as constants. First, in subsection 3.1 we will present the algorithm in a formal and abstract manner which is valid for any set of spatial coordinates. The algorithm,

based on the tridiagonal representation of the drift-kinetic equation, merges naturally when discretizing the velocity coordinate  $\xi$  using a Legendre spectral method. Nevertheless, for convenience, we will explain it in (right-handed) Boozer coordinates  $(\psi, \theta, \zeta) \in [0, \psi_{\text{lcs}}] \times [0, 2\pi) \times [0, 2\pi/N_p)$ . In these coordinates  $2\pi\psi$  is the toroidal flux of the magnetic field and  $\theta, \zeta$  are respectively the poloidal and toroidal (in a single period) angles. The integer  $N_p \geq 1$  denotes the number of periods of the device. In Boozer coordinates the magnetic field can be written as

$$\begin{aligned} \mathbf{B} &= \nabla\psi \times \nabla\theta - \iota(\psi) \nabla\psi \times \nabla\zeta \\ &= B_\psi(\psi, \theta, \zeta) \nabla\psi + B_\theta(\psi) \nabla\theta + B_\zeta(\psi) \nabla\zeta, \end{aligned} \quad (27)$$

and the Jacobian of the transformation reads

$$\sqrt{g}(\psi, \theta, \zeta) := (\nabla\psi \times \nabla\theta \cdot \nabla\zeta)^{-1} = \frac{B_\zeta + \iota B_\theta}{B^2}, \quad (28)$$

where  $\iota := \mathbf{B} \cdot \nabla\theta / \mathbf{B} \cdot \nabla\zeta$  is the rotational transform. The flux surface average operation (4) can be written in Boozer angles as

$$\langle f \rangle = \frac{dV^{-1}}{d\psi} \oint \oint f \sqrt{g} d\theta d\zeta. \quad (29)$$

We define§ the aforementioned reference value for the magnetic field strength  $B_0$  on the flux surface introduced in definition (16) as the  $(0, 0)$  Fourier mode of the magnetic field strength. Namely,

$$B_0(\psi) := \frac{1}{4\pi^2 N_p} \oint \oint B d\theta d\zeta. \quad (30)$$

Using (27) and (28), the spatial differential operators present in the drift-kinetic equation (18) can be expressed in these coordinates as

$$\mathbf{b} \cdot \nabla = \frac{B}{B_\zeta + \iota B_\theta} \left( \iota \frac{\partial}{\partial\theta} + \frac{\partial}{\partial\zeta} \right), \quad (31)$$

$$\mathbf{B} \times \nabla\psi \cdot \nabla = \frac{B^2}{B_\zeta + \iota B_\theta} \left( B_\zeta \frac{\partial}{\partial\theta} - B_\theta \frac{\partial}{\partial\zeta} \right). \quad (32)$$

After the explanation of the algorithm, in subsection 3.2 we explain how is implemented in MONKES.

#### 3.1. Legendre polynomial expansion

The algorithm is based on the approximate representation of the distribution function  $f$  in a truncated Legendre series. We will search for approximate solutions to equation (18) of the form

$$f(\theta, \zeta, \xi) = \sum_{k=0}^{N_\xi} f^{(k)}(\theta, \zeta) P_k(\xi), \quad (33)$$

§ Other definition could be, for example,  $\langle B \rangle$ . Nevertheless, both definitions are equal in the large aspect ratio limit.

where  $f^{(k)} = \langle f, P_k \rangle_{\mathcal{L}} / \langle P_k, P_k \rangle_{\mathcal{L}}$  is the  $k$ -th Legendre mode of  $f(\theta, \zeta, \xi)$  (see Appendix A) and  $N_\xi$  is an integer greater or equal to 1. As mentioned in Appendix A, the usage of the expansion on Legendre polynomials (33) ensures that the regularity conditions (12) are satisfied. Of course, in general, the exact solution to equation (18) does not have a finite Legendre spectrum, but taking  $N_\xi$  sufficiently high in expansion (33) yields an approximate solution to the desired degree of accuracy (in infinite precision arithmetic).

In Appendix A we derive explicitly the projection of each term of the drift-kinetic equation (18) onto the Legendre basis when the representation (33) is used. When doing so, we get that the Legendre modes of the drift-kinetic equation have the tridiagonal representation

$$L_k f^{(k-1)} + D_k f^{(k)} + U_k f^{(k+1)} = s^{(k)}, \quad (34)$$

for  $k = 0, 1, \dots, N_\xi$ , where we have defined for convenience  $f^{(-1)} := 0$  and from expansion (33) is clear that  $f^{(N_\xi+1)} = 0$ . Analogously to (33) the source term is expanded as  $s = \sum_{k=0}^{N_\xi} s^{(k)} P_k$ , and for the sources (19) this expansion is exact when  $N_\xi \geq 2$ . The spatial differential operators read

$$L_k = \frac{k}{2k-1} \left( \mathbf{b} \cdot \nabla + \frac{k-1}{2} \mathbf{b} \cdot \nabla \ln B \right), \quad (35)$$

$$D_k = -\frac{\hat{E}_\psi}{\langle B^2 \rangle} \mathbf{B} \times \nabla \psi \cdot \nabla + \frac{k(k+1)}{2} \hat{\nu}, \quad (36)$$

$$U_k = \frac{k+1}{2k+3} \left( \mathbf{b} \cdot \nabla - \frac{k+2}{2} \mathbf{b} \cdot \nabla \ln B \right). \quad (37)$$

Thanks to its tridiagonal structure, the system of equations (34) can be formally inverted using the standard Gaussian elimination algorithm for block tridiagonal matrices. Before introducing the algorithm we will explain how to fix the free constant of the solution to equation (34) so that it can be inverted. Note that the aforementioned nullspace of the drift-kinetic equation translates in the fact that  $f^{(0)}$  is not completely determined from equation (34). To prove this, we inspect the modes  $k = 0$  and  $k = 1$  that involve  $f^{(0)}$ . From expression (32) we can deduce that the term  $D_0 f^{(0)} + U_0 f^{(1)}$  is invariant if we add to  $f^{(0)}$  any function of  $B_\theta(\psi)\zeta + B_\zeta(\psi)\theta$  when  $\hat{E}_\psi \neq 0$  and does not include  $f^{(0)}$  for  $\hat{E}_\psi = 0$ . Besides, the term  $L_1 f^{(0)} + D_1 f^{(1)} + U_1 f^{(2)}$  remains invariant if we add to  $f^{(0)}$  any constant. Thus, equation (34) is unaltered when we add to  $f^{(0)}$  a constant. A constraint equivalent to condition (13) is to fix the value of the 0-th Legendre mode of the distribution function at a single point of the flux-surface. For example,

$$f^{(0)}(0, 0) = 0. \quad (38)$$

With this condition, equation (34) has a unique solution and can be inverted (further details on its invertibility are given in Appendix B) to obtain an approximation of the first  $N_\xi + 1$  Legendre modes of the solution to the drift-kinetic equation (18).

The algorithm for formally solving the truncated drift-kinetic equation (34) consists of two steps.

### (i) Forward elimination

Starting from  $\Delta_{N_\xi} = D_{N_\xi}$  and  $\sigma^{(N_\xi)} = s^{(N_\xi)}$  we can obtain recursively the operators

$$\Delta_k = D_k - U_k \Delta_{k+1}^{-1} L_{k+1}, \quad (39)$$

and the sources

$$\sigma^{(k)} = s^{(k)} - U_k \Delta_{k+1}^{-1} \sigma^{(k+1)}, \quad (40)$$

for  $k = N_\xi - 1, N_\xi - 2, \dots, 0$  (in this order). Equations (39) and (40) define the forward elimination. With this procedure we can transform equation (34) to the equivalent system

$$L_k f^{(k-1)} + \Delta_k f^{(k)} = \sigma^{(k)}, \quad (41)$$

for  $k = 0, 1, \dots, N_\xi$ . Note that this process corresponds to perform formal Gaussian elimination over

$$\left[ \begin{array}{ccc|c} L_k & D_k & U_k & s^{(k)} \\ 0 & L_{k+1} & \Delta_{k+1} & \sigma^{(k+1)} \end{array} \right], \quad (42)$$

to eliminate  $U_k$  in the first row.

### (ii) Backward substitution

Once we have the system of equations in the form (41) it is immediate to solve recursively

$$f^{(k)} = \Delta_k^{-1} \left( \sigma^{(k)} - L_k f^{(k-1)} \right), \quad (43)$$

for  $k = 0, 1, \dots, N_\xi$  (in this order). Here, we denote by  $\Delta_0^{-1} \sigma^{(0)}$  to the solution that satisfies (38). We recall that for  $k = 0$ , we must impose condition (38) so that  $\Delta_0 f^{(0)} = \sigma^{(0)}$  has a unique solution. As  $L_1 = \mathbf{b} \cdot \nabla$ , using expression (31), it is apparent from equation (43) that the integration constant does not affect the value of  $f^{(1)}$ .

We can apply this algorithm to solve equation (18) for  $f_1$ ,  $f_2$  and  $f_3$  in order to compute approximations to the transport coefficients. In terms of the Legendre modes of  $f_1$ ,  $f_2$  and  $f_3$ , the monoenergetic geometric coefficients from definition (26) read

$$\hat{D}_{11} = 2 \left\langle s_1^{(0)} f_1^{(0)} \right\rangle + \frac{2}{5} \left\langle s_1^{(2)} f_1^{(2)} \right\rangle, \quad (44)$$

$$\hat{D}_{31} = \frac{2}{3} \left\langle \frac{B}{B_0} f_1^{(1)} \right\rangle, \quad (45)$$

$$\hat{D}_{13} = 2 \left\langle s_1^{(0)} f_3^{(0)} \right\rangle + \frac{2}{5} \left\langle s_1^{(2)} f_3^{(2)} \right\rangle, \quad (46)$$

$$\hat{D}_{33} = \frac{2}{3} \left\langle \frac{B}{B_0} f_3^{(1)} \right\rangle, \quad (47)$$

where  $3s_1^{(0)}/2 = 3s_1^{(2)} = \mathbf{B} \times \nabla\psi \cdot \nabla B/B^3$ . Note from expressions (44), (45), (46) and (47) that, in order to compute the monoenergetic geometric coefficients  $\widehat{D}_{ij}$ , we only need to calculate the Legendre modes  $k = 0, 1, 2$  of the solution and we can stop the backward substitution (43) at  $k = 2$ . In the next subsection we will explain how MONKES approximately solves equation (34) using this algorithm.

### 3.2. Spatial discretization and algorithm implementation

The algorithm described above allows, in principle, to compute the exact solution to the truncated drift-kinetic equation (34) which is an approximate solution to (18). However, it is not possible, to our knowledge, to give an exact expression for the operator  $\Delta_k^{-1}$  except for  $k = N_\xi \geq 1$ . Instead, we are forced to compute an approximate solution to (34). In order to obtain an approximate solution of equation (34) we assume that each  $f^{(k)}$  has a finite Fourier spectrum so that it can be expressed as

$$f^{(k)}(\theta, \zeta) = \mathbf{I}(\theta, \zeta) \cdot \mathbf{f}^{(k)}, \quad (48)$$

where the Fourier interpolant row vector map  $\mathbf{I}(\theta, \zeta)$  is defined at Appendix C and the column vector  $\mathbf{f}^{(k)} \in \mathbb{R}^{N_{\text{fs}}}$  contains  $f^{(k)}$  evaluated at the equispaced grid points

$$\theta_i = 2\pi i/N_\theta, \quad i = 0, 1, \dots, N_\theta - 1, \quad (49)$$

$$\zeta_j = 2\pi j/(N_\zeta N_p), \quad j = 0, 1, \dots, N_\zeta - 1. \quad (50)$$

Here,  $N_{\text{fs}} := N_\theta N_\zeta$  is the number of points in which we discretize the flux surface being  $N_\theta$  and  $N_\zeta$  respectively the number of points in which we divide the domains of  $\theta$  and  $\zeta$ . The solution to equation (34) in general has an infinite Fourier spectrum and cannot exactly be written as (48), but taking  $N_\theta$  and  $N_\zeta$  sufficiently big, we can approximate the solution to equation (34) to arbitrary degree of accuracy (in infinite precision arithmetic). As is explained in Appendix C, introducing the Fourier interpolant (48) in equation (34) and then evaluating the result at the grid points, we obtain a system of  $N_{\text{fs}} \times (N_\xi + 1)$  equations which can be solved for  $\{\mathbf{f}^{(k)}\}_{k=0}^{N_\xi}$ . This system of equations is obtained by substituting the operators  $L_k, D_k, U_k$  in equation (34) by the  $N_{\text{fs}} \times N_{\text{fs}}$  matrices  $\mathbf{L}_k, \mathbf{D}_k, \mathbf{U}_k$ , defined in Appendix C. Thus, we discretize (34) as

$$\mathbf{L}_k \mathbf{f}^{(k-1)} + \mathbf{D}_k \mathbf{f}^{(k)} + \mathbf{U}_k \mathbf{f}^{(k+1)} = \mathbf{s}^{(k)}, \quad (51)$$

for  $k = 0, 1, \dots, N_\xi$ . Obviously, this system has a block tridiagonal structure and the algorithm presented in subsection 3.1 can be applied to it. We just have to replace in equations (39), (40) and (43) the operators and functions by their matrix and vector

analogues respectively. We will denote such matrix and vector analogues by boldface letters. The matrix approximation to the forward elimination procedure given by equations (39) and (40) reads

$$\Delta_k = \mathbf{D}_k - \mathbf{U}_k \Delta_{k+1}^{-1} \mathbf{L}_{k+1}, \quad (52)$$

$$\boldsymbol{\sigma}^{(k)} = \mathbf{s}^{(k)} - \mathbf{U}_k \Delta_{k+1}^{-1} \boldsymbol{\sigma}^{(k+1)}, \quad (53)$$

for  $k = N_\xi - 1, N_\xi - 2, \dots, 0$  (in this order). Thus, starting from  $\Delta_{N_\xi} = \mathbf{D}_{N_\xi}$  and  $\boldsymbol{\sigma}^{(N_\xi)} = \mathbf{s}^{(N_\xi)}$  all the matrices  $\Delta_k$  and the vectors  $\boldsymbol{\sigma}^{(k)}$  are defined from equations (52) and (53). Obtaining the matrix  $\Delta_k$  from equation (52) requires to invert  $\Delta_{k+1}$ , perform two matrix multiplications and a subtraction of matrices. The inversion using LU factorization and each matrix multiplication require  $O(N_{\text{fs}}^3)$  operations so it is desirable to reduce the number of matrix multiplications to one. For  $k \geq 2$ , we can reduce the number of matrix multiplications in determining  $\Delta_k$  to one if instead of computing  $\Delta_{k+1}^{-1}$  we solve for  $\mathbf{X}_{k+1}$  the matrix system of equations

$$\Delta_{k+1} \mathbf{X}_{k+1} = \mathbf{L}_{k+1}, \quad (54)$$

and then obtain

$$\Delta_k = \mathbf{D}_k - \mathbf{U}_k \mathbf{X}_{k+1}, \quad (55)$$

for  $k = N_\xi - 1, N_\xi - 2, \dots, 2$ . For  $k \leq 1$  as we need to solve (41) and do the backward substitution (43), it is convenient to compute and store  $\Delta_k^{-1}$ . Besides, as none of the source terms  $s_1, s_2$  and  $s_3$  given by (19) have Legendre modes greater than 2 we have from equation (53) that  $\boldsymbol{\sigma}^{(k)} = 0$  for  $k \geq 3$  and  $\boldsymbol{\sigma}^{(2)} = \mathbf{s}^{(2)}$  and (53) must be applied just when  $k = 0$  and  $k = 1$ . Applying once (53) requires  $O(N_{\text{fs}}^2)$  operations and its contribution to the arithmetic complexity of the algorithm is subdominant with respect to the matrix inversions and multiplications. As the resolution of a matrix system of equations and matrix multiplication must be done  $N_\xi + 1$  times, solving equation (51) by this method requires  $O(N_\xi N_{\text{fs}}^3)$  operations.

In what concerns to memory resources, as we are only interested in the Legendre modes 0, 1 and 2, it is not necessary to store in memory all the matrices  $\mathbf{L}_k, \mathbf{D}_k, \mathbf{U}_k$  and  $\Delta_k$ . Instead, we store solely  $\mathbf{L}_k, \mathbf{U}_k$  and  $\Delta_k^{-1}$  for  $k = 0, 1, 2$ . For the intermediate steps we just need to use some auxiliary matrices  $\mathbf{L}, \mathbf{D}, \mathbf{U}, \Delta$  and  $\mathbf{X}$ . This makes the amount of memory required by MONKES independent of  $N_\xi$ .

To summarize, the pseudocode of the implementation of the algorithm in MONKES is given in Algorithm 1. In the first loop from  $k = N_\xi - 1$  to  $k = 2$  we construct  $\mathbf{L}_2, \Delta_2^{-1}$  and  $\mathbf{U}_2$  without saving any matrix from the intermediate steps nor computing any vector  $\boldsymbol{\sigma}^{(k)}$ . After that, in the second loop from  $k = 1$  to  $k = 0$ , the

---

**Algorithm 1** Block tridiagonal solution algorithm implemented in MONKES.

---

Forward elimination:

```

 $L \leftarrow L_{N_\xi}$  ▷ Starting value for  $L$ 
 $\Delta \leftarrow D_{N_\xi}$  ▷ Starting value for  $\Delta$ 
for  $k = N_\xi - 1$  to 2 do
  Solve  $\Delta X = L$  ▷ Compute  $X_{k+1}$  stored in  $X$ 
   $L \leftarrow L_k$  ▷ Construct  $L_k$  stored in  $L$ 
   $D \leftarrow D_k$  ▷ Construct  $D_k$  stored in  $D$ 
   $U \leftarrow U_k$  ▷ Construct  $U_k$  stored in  $U$ 
   $\Delta \leftarrow D - UX$  ▷ Construct  $\Delta_k$  stored in  $\Delta$ 
  if  $k = 2$  then ▷ Save required matrices
     $L_k \leftarrow L$  ▷ Save  $L_2$ 
    Solve  $\Delta \Delta_k^{-1} = \text{Identity}$  ▷ Compute  $\Delta_2^{-1}$ 
     $U_k \leftarrow U$  ▷ Save  $U_2$ 
  end if
end for
for  $k = 1$  to 0 do
  if  $k > 0$   $L_k \leftarrow L_k$  ▷ Construct and save  $L_k$ 
   $D \leftarrow D_k$  ▷ Construct  $D_k$  stored in  $D$ 
   $U_k \leftarrow U_k$  ▷ Construct and save  $U_k$ 
   $\Delta_k^{-1} \leftarrow D - U_k \Delta_{k+1}^{-1} L_k$  ▷ Construct  $\Delta_k$ 
   $\sigma^{(k)} \leftarrow s^{(k)} - U_k \Delta_{k+1}^{-1} \sigma^{(k+1)}$  ▷ Construct  $\sigma^{(k)}$ 
  Solve  $\Delta \Delta_k^{-1} = \text{Identity}$  ▷ Compute  $\Delta_k^{-1}$ 
end for

```

Backward substitution:

```

 $f^{(0)} \leftarrow \Delta_0^{-1} \sigma^{(0)}$ 
for  $k = 1$  to 2 do
   $f^{(k)} \leftarrow \Delta_k^{-1} (\sigma^{(k)} - L_k f^{(k-1)})$ 
end for

```

---

matrices  $L_k$  and  $\Delta_k^{-1}$  are computed and saved for the posterior step of backward substitution.

Once we have solved (51) for  $f^{(0)}$ ,  $f^{(1)}$  and  $f^{(2)}$ , the integrals of the flux surface average operation involved in the geometric coefficients (44), (45), (46) and (47), are conveniently computed using the trapezoidal rule, which for periodic analytic functions has geometric convergence [35]. In the next sections we will see that despite the cubic scaling in  $N_{fs}$  of the arithmetical complexity of the algorithm, it is possible to obtain fast and accurate calculations of the monoenergetic geometric coefficients at low collisionality (in particular  $\hat{D}_{31}$ ) in a single processor. The reason behind this is that in the asymptotic relation  $O(N_{fs}^3) \sim C_{alg} N_{fs}^3$ , the constant  $C_{alg}$  is small enough to allow  $N_{fs}$  to take a value sufficiently high to capture accurately the spatial dependence of the distribution function without increasing much the wall-clock time. The algorithm is implemented in the new code MONKES, written in Fortran language. The matrix inversions and multiplications are computed using the linear algebra library LAPACK [36].

## 4. Numerical results and benchmark

In this section we will demonstrate how MONKES provides fast and accurate calculations of the monoenergetic coefficients from low ( $\hat{\nu} = 10^{-5} \text{ m}^{-1}$ ) to high collisionality ( $\hat{\nu} = 3 \cdot 10^2 \text{ m}^{-1}$ ) benchmarked with DKES and for some cases in which DKES calculations are not accurate, also with SFINCS. In first place, for the sake of clarity, we will translate our parameters ( $\hat{\nu}, \hat{E}_\psi$ ) to match the normalization of DKES output. The quantity  $\hat{\nu}$  is called CMUL in the code DKES. For the electric field,  $\hat{E}_\psi$  is related to the variable EFIELD from DKES via  $\text{EFIELD} = \hat{E}_\psi d\psi/dr$  where  $r^2/L_a^2 = \psi/\psi_{lcs}$  and  $L_a$  is the minor radius of the device. We will denote this quantity by  $\hat{E}_r := \hat{E}_\psi d\psi/dr$ .

It is convenient to check that the arithmetic complexity of the algorithm describe in section 3 holds in practice. As can be seen on figure 1, the code scales linearly with the number of Legendre modes  $N_\xi$  and cubically with the number of points in which the flux surface is discretized  $N_{fs}$ . As was mentioned at the end of section 3, the constant  $C_{alg}$  in a single processor is sufficiently small to give accurate calculations up to  $\hat{\nu} \sim 10^{-5} \text{ m}^{-1}$ . We will see in this section that the number of points required for a correct calculation of the monoenergetic coefficients for  $\hat{\nu} \geq 10^{-5}$  are below 2000 points and less than 200 Legendre modes. We can see from figure 1 that for  $N_{fs} \simeq 2000$  the wall-clock time per Legendre mode in a single processor is approximately 0.6 s. For this spatial resolution, using 200 Legendre modes produces calculations in 2 minutes. For accurate evaluation of the monoenergetic coefficients in the cases selected, it will require approximately 1 minute. Finally, we inform that the wall-clock times for all the calculations shown are those from one of the partitions of CIEMAT's cluster XULA. Specifically, in partition number 2¶ whose nodes run with Intel Xeon Gold 6254 cores at 3.10 GHz.

### 4.1. Convergence of monoenergetic coefficients at low collisionality

At the low collisionality regime, convection is dominant with respect to diffusion. As equation (18) is singularly perturbed with respect to  $\hat{\nu}$ , its solution posses internal boundary layers in  $\xi$ . These boundary layers appear at the interfaces between different classes of trapped particles. At these regions of phase space, collisions are no longer subdominant with respect to the advection.

¶ In this context “accurate at high collisionality” means that the drift-kinetic equation (18) is solved accurately, without considering the incorrectness of the collision operator used.

¶ Partition number 1 nodes use Intel Xeon Gold 6148 cores which run at 2.4 GHz. Typically it has been found that this partition is 1.1-1.2 times faster. Nevertheless, in order to be conservative, we show MONKES results on the slower cores.



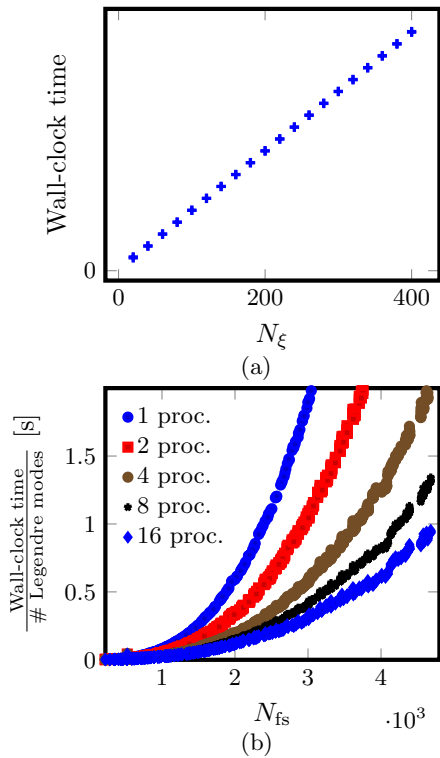


Figure 1: Scaling of MONKES computation time with the resolutions. (a) Linear scaling with the number of Legendre modes. (b) Cubic scaling with  $N_{fs}$  for different number of processors used.

Also at these regions, the poloidal  $\mathbf{E} \times \mathbf{B}$  precession from equation (18) can produce the chaotic transition of collisionless particles from one class to another due to separatrix crossing mechanisms [37]. The existence of these localized regions with large  $\xi$  gradients forces to take a truncated expansion with a high number of Legendre modes  $N_\xi$ , explaining the difficulty to obtain fast and accurate solutions to equation (18) at low collisionality.

In this subsection we will demonstrate that MONKES can provide fast and accurate calculations of the monoenergetic coefficients at a wide range of collisionalities. For this, we will study how the monoenergetic coefficients computed by MONKES converge with  $N_\theta$ ,  $N_\zeta$  and  $N_\xi$  at the low collisionality regime. From the point of view of numerical analysis, it is the lack of diffusion along  $\xi$  in equation (18) the responsible for the necessity of large values of  $N_\xi$ . Hence, if MONKES is capable of producing fast and accurate calculations at low collisionality, is safe to assume that it will also produce fast and accurate calculations at higher collisionalities. For the convergence study, we select three different magnetic configurations at a single flux surface. Two of them correspond to two modes of operation of W7-

Configuration	$\psi/\psi_{lfs}$	$\hat{\nu}$ [ $m^{-1}$ ]	$\hat{E}_r$ [ $kV \cdot s/m^2$ ]
W7X-EIM	0.200	$10^{-5}$	0
W7X-EIM	0.200	$10^{-5}$	$3 \cdot 10^{-4}$
W7X-KJM	0.204	$10^{-5}$	0
W7X-KJM	0.204	$10^{-5}$	$3 \cdot 10^{-4}$
CIEMAT-QI	0.250	$10^{-5}$	0
CIEMAT-QI	0.250	$10^{-5}$	$10^{-3}$

Table 1: Cases considered to study the convergence of monoenergetic coefficients and values of  $(\hat{\nu}, \hat{E}_r)$ .

X: EIM and KJM. The third one corresponds to the new QI “flat mirror” [7] configuration CIEMAT-QI [6]. This selection of cases mimics what types of magnetic configurations will need to be evaluated when optimizing QI stellarators. Starting from W7-X EIM, at the middle of the optimization process, a magnetic configuration similar to W7-X KJM might be found. At the end of the optimization process, the final magnetic field an optimized QI configuration such as CIEMAT-QI would need to be evaluated. The calculations are done for the  $1/\nu$  ( $\hat{E}_r = 0$ ) and  $\sqrt{\nu}$  regimes at the low collisionality value  $\hat{\nu} = 10^{-5}$ . In table 1 the list of cases considered is enlisted with their correspondent values of  $\hat{E}_r$ .

For each configuration we will proceed in the same manner. First, we plot the coefficients  $\hat{D}_{ij}$  as functions of the number of Legendre modes in a sufficiently wide interval. For each value of  $N_\xi$  the selected spatial resolutions  $N_\theta$  and  $N_\zeta$  are sufficiently large so that increasing them varies the monoenergetic coefficients in less than a 1%. We will call this situation “spatially converged”. From the curve of (spatially converged)  $\hat{D}_{31}$  as a function of  $N_\xi$  we define our converged reference value, which we denote by  $\hat{D}_{31}^r$ , as the converged calculation to three significant digits. From this converged reference value we will define two regions. A first region

$$\mathcal{R}_\epsilon := [(1 - \epsilon/100)\hat{D}_{31}^r, (1 + \epsilon/100)\hat{D}_{31}^r] \quad (56)$$

for calculations that deviate less than or equal to an  $\epsilon\%$  with respect to  $\hat{D}_{31}^r$ . The second interval

$$\mathcal{A}_\epsilon := [\hat{D}_{31}^r - \epsilon, \hat{D}_{31}^r + \epsilon] \quad (57)$$

is for calculations which are at a distance less or equal to  $\epsilon$ . The reason to have two different regions is that for stellarators close to QI, the relative convergence criteria can be too demanding as the smaller is  $\hat{D}_{31}^r$ , the narrower  $\mathcal{R}_\epsilon$  becomes. Nevertheless, for optimization purposes, it is sufficient to ensure that  $|\hat{D}_{31}|$  is sufficiently small. If we optimize for quasi-isodynamicity using a value  $\hat{D}_{31} = \hat{D}_{31}^r + \epsilon \in \mathcal{A}_\epsilon$ , and for the optimized stellarator  $\hat{D}_{31} = 0$ , then it

is reasonable to expect that the converged value is consequently small  $|\hat{D}_{31}^r| \sim |\epsilon|$ . We will use this interval for two purposes: first to give a visual idea of how narrow  $\mathcal{R}_\epsilon$  becomes. Secondly, to show how in the case in which calculations are less fast, it is easier to satisfy an absolute criteria than a relative one.

As typically the most difficult coefficient to compute is the bootstrap current coefficient, we will select the resolutions so that  $\hat{D}_{31}$  is accurately computed. In order to select the triplets  $(N_\theta, N_\zeta, N_\xi)$  for “sufficiently accurate” calculations of  $\hat{D}_{31}$ , we need to define properly what it means to be “sufficiently converged”. For this, we will use the relative convergence region. We say that, for fixed  $(N_\theta, N_\zeta, N_\xi)$  and  $\epsilon$ , a calculation  $\hat{D}_{31} \in \mathcal{R}_\epsilon$  is sufficiently converged if, two conditions are satisfied

- (i) Spatially converged calculations with  $N'_\xi > N_\xi$  still belong to  $\mathcal{R}_\epsilon$ .
- (ii) Increasing  $N_\theta$  and  $N_\zeta$  keeping  $N_\xi$  constant produces calculations which belong to  $\mathcal{R}_\epsilon$ .

Condition (i) is used to select the number of Legendre modes  $N_\xi$  and condition (ii) is used to select the values of  $N_\theta$  and  $N_\zeta$  once  $N_\xi$  is fixed.

On figure 2 the convergence of monoenergetic coefficients with the number of Legendre modes is shown for W7-X EIM in the  $1/\nu$  regime. From figures 2a and 2b we see that the radial transport and parallel conductivity coefficients converge monotonically with  $N_\xi$ . On the other hand, the bootstrap current coefficient is more difficult to converge as can be seen on 2c. The converged reference value  $\hat{D}_{31}^r$  taken is the spatially converged calculation for  $N_\xi = 380$ . Defining a region of relative convergence of  $\epsilon = 5\%$ , allows to select a resolution of  $N_\xi = 140$  Legendre modes to satisfy condition (i). From figure 2d we choose the resolutions  $(N_\theta, N_\zeta) = (23, 55)$  to satisfy convergence condition (ii). The selected calculation is indicated with a green five-point star, and the wall-clock time spent is of 22 seconds.

For the  $\sqrt{\nu}$  regime case of W7-X EIM on figure 3c we check that the calculation for  $N_\xi = 300$  serves as converged reference value  $\hat{D}_{31}^r$ . On figure 3c we notice that to obtain sufficiently converged results for the region  $\mathcal{R}_5$  is more difficult than in the previous  $1/\nu$  regime. This is in part due to the fact that the  $\hat{D}_{31}$  coefficient is smaller in absolute value and thus, the region  $\mathcal{R}_5$  is narrower. We select  $N_\xi = 160$  (indicated again with a green star) to satisfy condition (i). The selection  $(N_\theta, N_\zeta) = (27, 55)$  satisfies condition (ii) as shown in figure 3d. With this selection of  $(N_\theta, N_\zeta, N_\xi)$  it required 40 seconds to compute the monoenergetic coefficients, which is quite fast.

For the high mirror configuration of W7-X in the  $1/\nu$  we use the calculation for  $N_\xi = 380$  as the

converged reference value  $\hat{D}_{31}^r$  as shown in figure 4c. Due to the smaller value of  $\hat{D}_{31}^r$  the amplitude of the region  $\mathcal{R}_5$  is much narrower, being of order  $10^{-3}$ . On figure 4c we see that taking  $N_\xi = 140$  is sufficient to satisfy condition (i). According to the convergence curves shown in figure 4d, taking  $(N_\theta, N_\zeta) = (23, 63)$  would yield a calculation that satisfies condition (ii). This calculation is also quite fast, with a wall-clock time of 33 seconds.

For W7-X KJM in the  $\sqrt{\nu}$  regime the calculation for  $N_\xi = 340$  serves as the converged reference value  $\hat{D}_{31}^r$  as shown on figure 4c. The selection of Legendre modes  $N_\xi = 180$  to have a calculation which satisfies convergence condition (i) is indicated with a green star on figure 5c. Condition (ii) is satisfied by the selection  $(N_\theta, N_\zeta) = (19, 79)$ , as shown on figure 5d. This calculation is also fast, taking 46 seconds.

The convergence of monoenergetic coefficients for the nearly quasi-isodynamic configuration CIEMAT-QI in the  $1/\nu$  regime is shown in figure 6. From figure 6c we see that the calculation for  $N_\xi = 400$  is used as the converged reference value  $\hat{D}_{31}^r$  and we relax the relative convergence parameter to  $\epsilon = 7\%$ . On figure 6c we see that the region of 7% of deviation  $\mathcal{R}_7$  is quite narrow and that selecting  $N_\xi = 180$  satisfies condition (i). To satisfy condition (ii) we choose the resolutions  $(N_\theta, N_\zeta) = (15, 119)$  as shown in figure 6d. Again, the calculation with the selected resolutions is fast, taking 78 seconds.

For CIEMAT-QI in the  $\sqrt{\nu}$  regime, we take the calculation for  $N_\xi = 380$  as the converged reference value  $\hat{D}_{31}^r$  as shown on figure 7. From figure 7c we can check that taking  $N_\xi = 180$  satisfies condition (i) for the region  $\mathcal{R}_7$  of 7% of deviation. As shown in figure 7d, the selection  $(N_\theta, N_\zeta) = (15, 119)$  satisfies condition (ii). With this selection, which is the same as for the  $1/\nu$  regime, we obtain the same wall-clock time of 78 seconds.

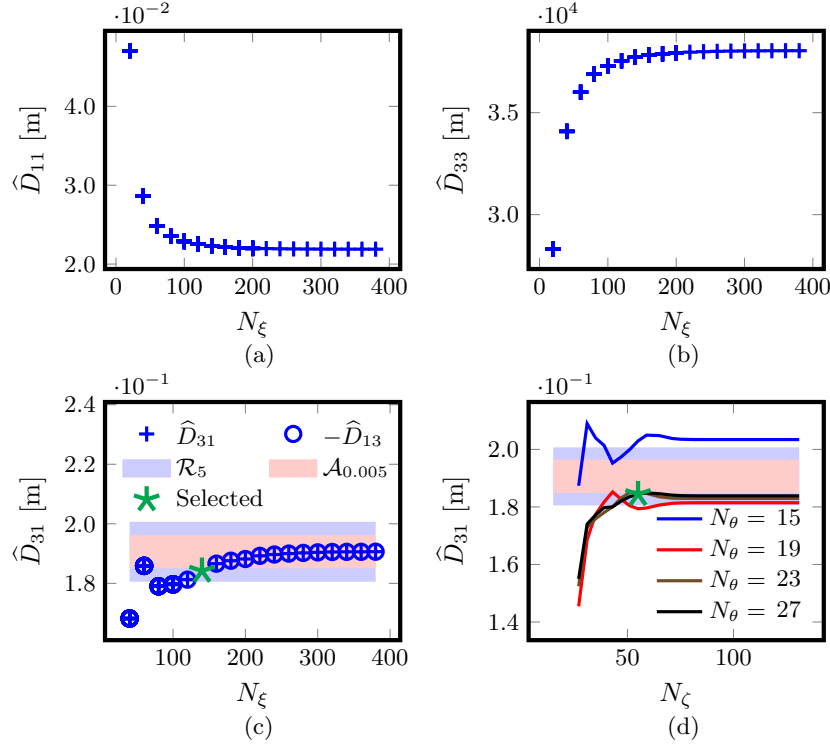


Figure 2: Convergence of monoenergetic coefficients with the number of Legendre modes  $N_\xi$  for W7X-EIM at the surface labelled by  $\psi/\psi_{\text{lfs}} = 0.200$ , for  $\hat{\nu}(v) = 10^{-5} \text{ m}^{-1}$  and  $\hat{E}_r(v) = 0 \text{ kV} \cdot \text{s/m}^2$ .

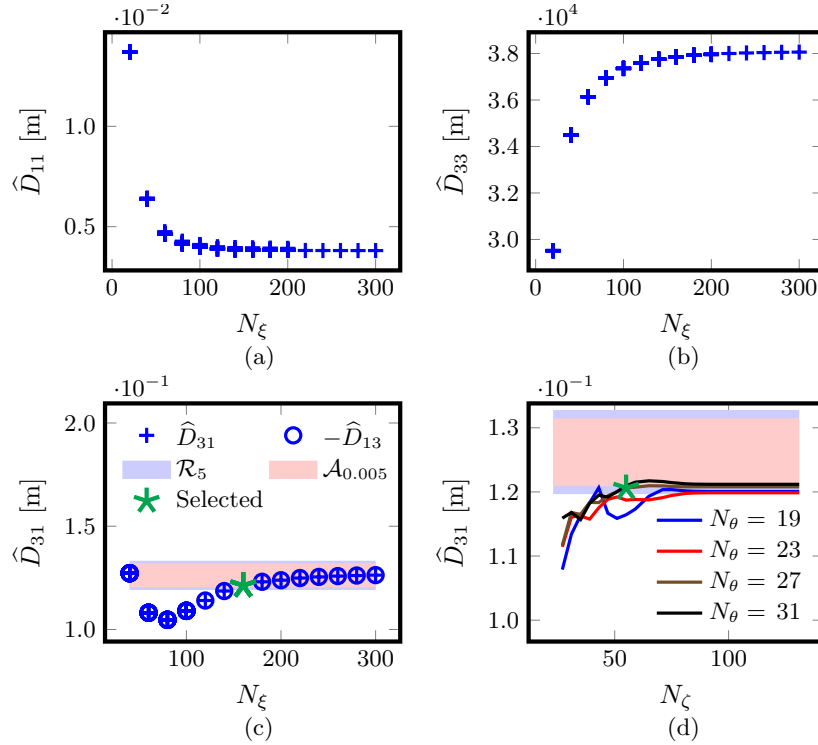


Figure 3: Convergence of monoenergetic coefficients with the number of Legendre modes  $N_\xi$  for W7X-EIM at the surface labelled by  $\psi/\psi_{\text{lfs}} = 0.200$ , for  $\hat{\nu}(v) = 10^{-5} \text{ m}^{-1}$  and  $\hat{E}_r = 3 \cdot 10^{-4} \text{ kV} \cdot \text{s/m}^2$ .

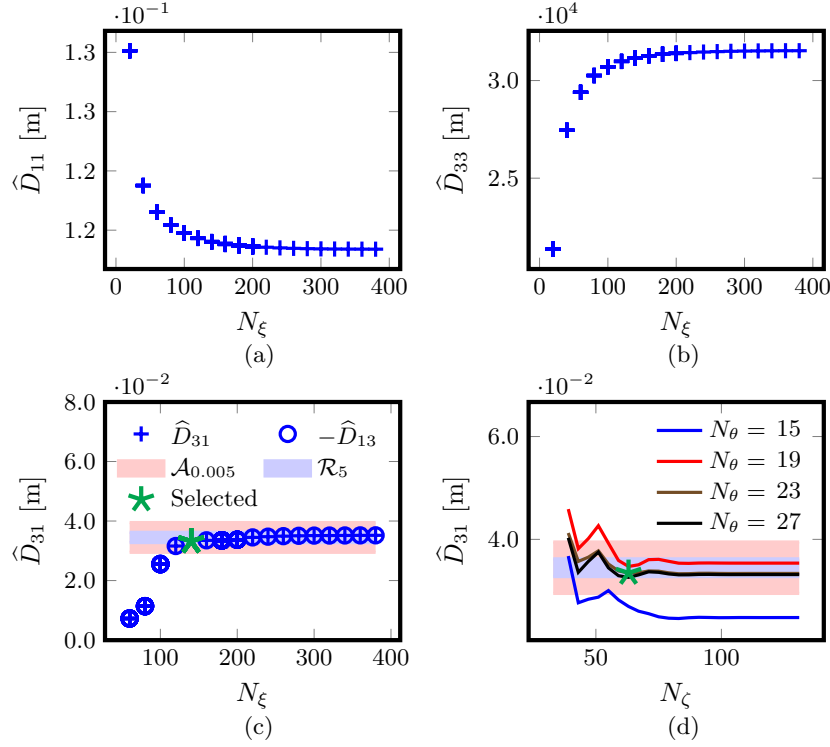


Figure 4: Convergence of monoenergetic coefficients with the number of Legendre modes  $N_\xi$  for W7X-KJM at the surface labelled by  $\psi/\psi_{\text{lfs}} = 0.204$ , for  $\hat{\nu}(v) = 10^{-5} \text{ m}^{-1}$  and  $\hat{E}_r(v) = 0 \text{ kV} \cdot \text{s/m}^2$ .

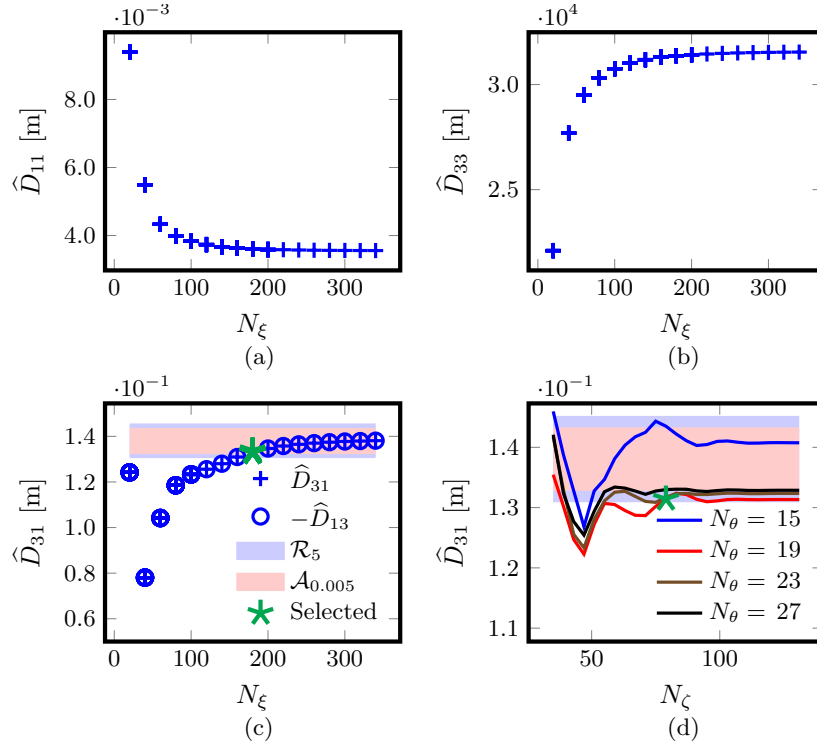


Figure 5: Convergence of monoenergetic coefficients with the number of Legendre modes  $N_\xi$  for W7X-KJM at the surface labelled by  $\psi/\psi_{\text{lfs}} = 0.204$ , for  $\hat{\nu}(v) = 10^{-5} \text{ m}^{-1}$  and  $\hat{E}_r(v) = 3 \cdot 10^{-4} \text{ kV} \cdot \text{s/m}^2$ .

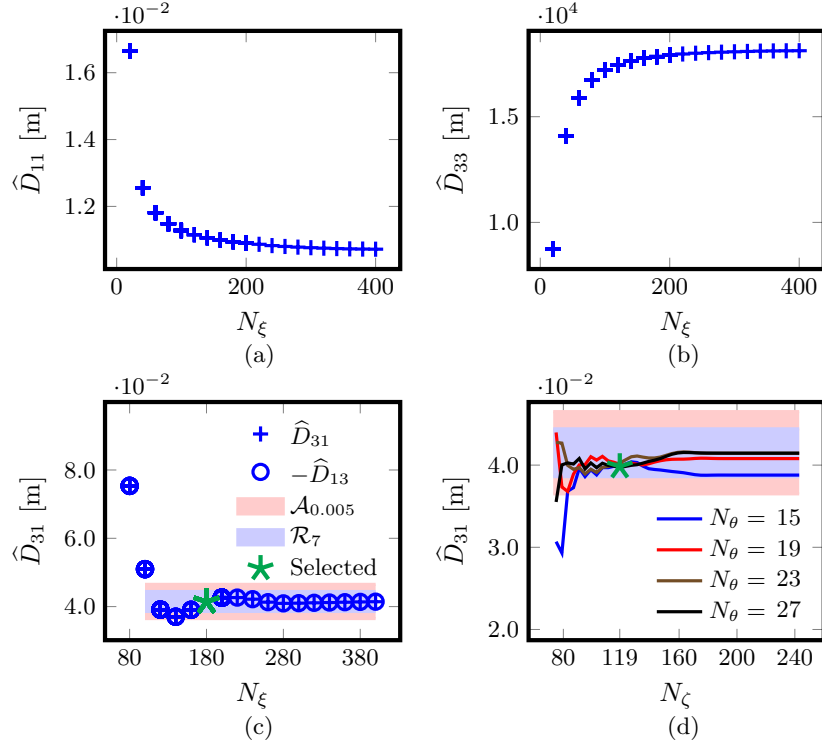


Figure 6: Convergence of monoenergetic coefficients with the number of Legendre modes  $N_\xi$  for CIEMAT-QI at the surface labelled by  $\psi/\psi_{\text{lfs}} = 0.25$ , for  $\hat{\nu}(v) = 10^{-5} \text{ m}^{-1}$  and  $\hat{E}_r(v) = 0 \text{ kV} \cdot \text{s/m}^2$ .

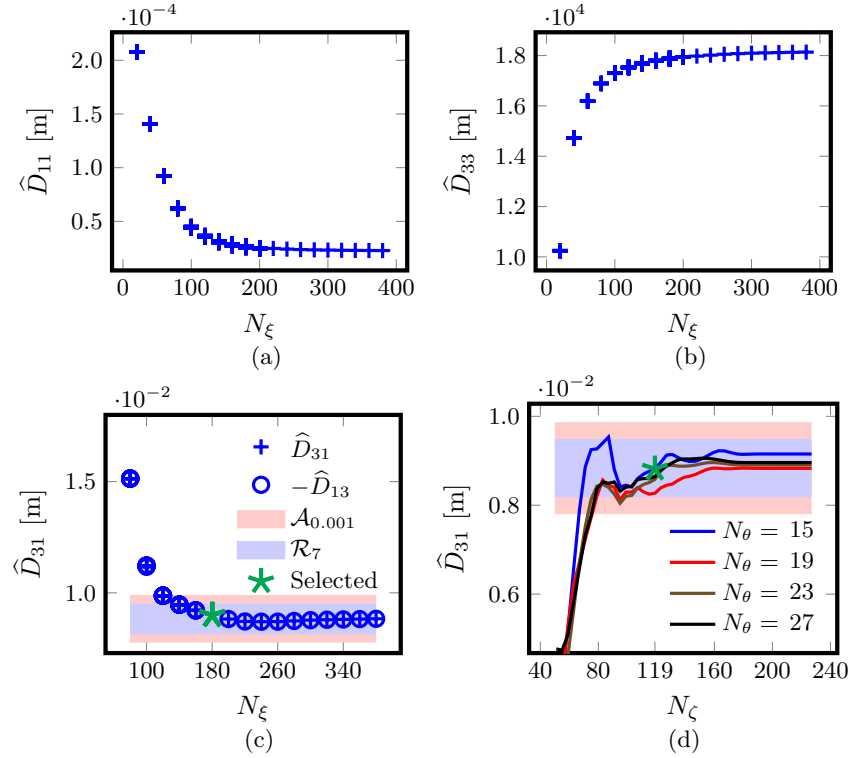


Figure 7: Convergence of monoenergetic coefficients with the number of Legendre modes  $N_\xi$  for CIEMAT-QI at the surface labelled by  $\psi/\psi_{\text{lfs}} = 0.25$ , for  $\hat{\nu}(v) = 10^{-5} \text{ m}^{-1}$  and  $\hat{E}_r(v) = 10^{-3} \text{ kV} \cdot \text{s/m}^2$ .

For the wall-clock time comparison and the benchmark of the next subsection, a similar convergence study has been carried out with DKES on Appendix D. On figures D1, D2 and D3 from Appendix D, the convergence with the number of Legendre modes of the monoenergetic coefficients calculated by DKES is shown. Additionally, on figures D1b, D1e, D2b, D2e, D3b and D3e we plot the regions of convergence  $\mathcal{R}_\epsilon$  for each case. This is done to compare the wall-clock times between MONKES and DKES for the same level of relative convergence with respect to  $\hat{D}_{31}^r$ . This comparison is displayed on table 2. In all three cases, MONKES is faster than DKES despite using more Legendre modes. Even for W7-X EIM, in which we have taken  $N_\xi = 80$  for DKES calculations, MONKES is faster using twice the number of Legendre modes. For the high mirror configuration, MONKES is  $\sim 20$  times faster than DKES in the  $1/\nu$  regime and  $\sim 7$  times faster than DKES in the  $\sqrt{\nu}$  regime. In the case of CIEMAT-QI, MONKES is not only  $\sim 3$  times faster but we will see it is also much more accurate.

TABLE. COLUMNS: Case, t1p, t2p, t4p, t8p, t16p

Case	$N_\xi^{\text{DKES}}$	$\epsilon\%$	$t_{\text{clock}}^{\text{DKES}}$ [s]	$t_{\text{clock}}^{\text{MONKES}}$ [s]
W7X-EIM $1/\nu$	80		83.9	22
W7X-EIM $\sqrt{\nu}$	80		57.5	40
W7X-KJM $1/\nu$	120		615	33
W7X-KJM $\sqrt{\nu}$	60		248	46
CIEMAT-QI $1/\nu$	100		238	78
CIEMAT-QI $\sqrt{\nu}$	120		214	78

Table 2: Minimum number of Legendre modes for DKES results to satisfy convergence conditions (i) and (ii) and comparison between the wall-clock time of DKES and MONKES.

#### 4.2. Benchmark of monoenergetic coefficients

### 5. Conclusions and future work

#### Appendix A. Legendre modes of the drift-kinetic equation

Legendre polynomials are the eigenfunctions of the Sturm-Liouville problem in the interval  $\xi \in [-1, 1]$  defined by the differential equation

$$2\mathcal{L}P_k(\xi) = -k(k+1)P_k(\xi), \quad (\text{A.1})$$

and regularity boundary conditions at  $\xi = \pm 1$

$$(1 - \xi^2) \frac{dP_k}{d\xi} \Big|_{\xi=\pm 1} = 0, \quad (\text{A.2})$$

where  $k \geq 0$  is an integer.

As  $\mathcal{L}$  has a discrete spectrum and is self-adjoint with respect to the inner product

$$\langle f, g \rangle_{\mathcal{L}} := \int_{-1}^1 fg d\xi, \quad (\text{A.3})$$

in the space of functions that satisfy the regularity condition,  $\{P_k\}_{k=0}^\infty$  is an orthogonal basis satisfying  $\langle P_j, P_k \rangle_{\mathcal{L}} = 2\delta_{jk}/(2k+1)$ . Hence, these polynomials satisfy the three-term recurrence formula

$$(2k+1)\xi P_k(\xi) = (k+1)P_{k+1}(\xi) + kP_{k-1}(\xi), \quad (\text{A.4})$$

obtained by Gram-Schmidt orthogonalization, which starting from  $P_0 = 1$  and  $P_1 = \xi$  defines them all. Additionally, they satisfy the differential identity

$$(1 - \xi^2) \frac{dP_k}{d\xi} = kP_{k-1}(\xi) - k\xi P_k(\xi). \quad (\text{A.5})$$

Identities (A.4) and (A.5) are useful to represent tridiagonally the left-hand side of equation (18) when we use the expansion (33). The  $k$ -th Legendre mode of the term  $\xi \mathbf{b} \cdot \nabla f$  is expressed in terms of the modes  $f^{(k-1)}$  and  $f^{(k+1)}$  using (A.4)

$$\langle \xi \mathbf{b} \cdot \nabla f, P_k \rangle_{\mathcal{L}} = \frac{2}{2k+1} \left[ \frac{k}{2k-1} \mathbf{b} \cdot \nabla f^{(k-1)} + \frac{k+1}{2k+3} \mathbf{b} \cdot \nabla f^{(k+1)} \right]. \quad (\text{A.6})$$

Combining both (A.4) and (A.5) allows to express the  $k$ -th Legendre mode of the mirror term  $\nabla \cdot \mathbf{b}((1 - \xi^2)/2) \partial f / \partial \xi$  in terms of the modes  $f^{(k-1)}$  and  $f^{(k+1)}$  as

$$\left\langle \frac{1}{2}(1 - \xi^2) \nabla \cdot \mathbf{b} \frac{\partial f}{\partial \xi}, P_k \right\rangle_{\mathcal{L}} = \frac{\mathbf{b} \cdot \nabla \ln B}{2k+1} \left[ \frac{k(k-1)}{2k-1} f^{(k-1)} - \frac{(k+1)(k+2)}{2k+3} f^{(k+1)} \right], \quad (\text{A.7})$$

where we have also used  $\nabla \cdot \mathbf{b} = -\mathbf{b} \cdot \nabla \ln B$ . The term proportional to  $\hat{E}_\psi$  is diagonal in a Legendre representation

$$\left\langle \frac{\hat{E}_\psi}{\langle B^2 \rangle} \mathbf{B} \times \nabla \psi \cdot \nabla f, P_k \right\rangle_{\mathcal{L}} = \quad (\text{A.8})$$

$$\frac{2}{2k+1} \frac{\hat{E}_\psi}{\langle B^2 \rangle} \mathbf{B} \times \nabla \psi \cdot \nabla f^{(k)}.$$

Finally, for the collision operator used in equation (18), as Legendre polynomials are eigenfunctions of the pitch-angle scattering operator, using (A.1) we obtain the diagonal representation

$$\langle \hat{\nu} \mathcal{L} f, P_k \rangle_{\mathcal{L}} = -\hat{\nu} \frac{k(k+1)}{2k+1} f^{(k)}. \quad (\text{A.9})$$

## Appendix B. Invertibility of the spatial differential operators

In this Appendix we will study the invertibility of the left-hand-side of (34). For this, we view  $L_k$ ,  $D_k$  and  $U_k$  as operators from  $\mathcal{F}$  to  $\mathcal{F}$ , where  $\mathcal{F}$  is the space of smooth functions on the flux-surface equipped with the inner product

$$\langle f, g \rangle_{\mathcal{F}} = \frac{N_p}{4\pi^2} \oint \oint f \bar{g} d\theta d\zeta, \quad (\text{B.1})$$

where  $\bar{z}$  denotes the complex conjugate of  $z$  and the induced norm

$$\|f\|_{\mathcal{F}} := \sqrt{\langle f, f \rangle_{\mathcal{F}}}. \quad (\text{B.2})$$

In this setting  $L_k$ ,  $D_k$  and  $U_k$  are bounded operators from  $\mathcal{F}$  to  $\mathcal{F}$  as all the coefficients are smooth. The operators  $L_k$  and  $U_k$  given by (35) and (37) do not have a uniquely defined inverse as they have a non zero kernel. This is a consequence of the fact that the parallel streaming operator

$$\mathcal{V}_{\parallel} = \xi \mathbf{b} \cdot \nabla + \nabla \cdot \mathbf{b} \frac{(1 - \xi^2)}{2} \frac{\partial}{\partial \xi} \quad (\text{B.3})$$

has a kernel consisting of functions  $g((1 - \xi^2)/B)$ .

To study the invertibility of  $L_k$  and  $U_k$  we employ coordinates  $(\alpha, l)$  where  $\alpha$  is a poloidal angle that labels field lines and  $l$  is the magnetic field length. Note that we can study the invertibility of  $L_k$  and  $U_k$  by studying the existence of solutions to

$$\frac{dh}{dl} + a(\alpha, l)h = s(\alpha, l), \quad (\text{B.4})$$

where  $a(\alpha, l)$  and  $s(\alpha, l)$  are smooth functions. It is easy to check that the general solution to (B.4) can be written as

$$h(\alpha, l) = (h_0(\alpha) + W(\alpha, l)) \exp(-A(\alpha, l)), \quad (\text{B.5})$$

where

$$A(\alpha, l) = \int_0^l a(\alpha, l') dl', \quad (\text{B.6})$$

and

$$W(\alpha, l) = \int_0^l s(\alpha, l') \exp(A(\alpha, l')) dl' \quad (\text{B.7})$$

satisfying  $h(\alpha, 0) = h_0(\alpha)$ . Thus, the solution to (B.4) in the plane  $(\alpha, l)$  is determined up to a constant  $h_0(\alpha)$ . Imposing continuity on the flux surface to solution (B.5) fixes under some circumstances for  $a(\alpha, l)$ , the constant  $h_0$ . When  $\iota$  is rational the field line closes on itself after a length  $L$ , thus continuity imposes  $h(\alpha, l + L) = h(\alpha, l)$ . In particular, continuity at  $l = 0$  imposes

$$h_0(\alpha) = (h_0(\alpha) + W(\alpha, L)) \exp(-A(\alpha, L)). \quad (\text{B.8})$$

If  $A(\alpha, L) \neq 0$ , continuity condition (B.8) fixes the value of  $h_0(\alpha)$  as

$$h_0(\alpha) = W(\alpha, L) \frac{\exp(-A(\alpha, L))}{1 - \exp(-A(\alpha, L))} \quad (\text{B.9})$$

An equivalent manner to fix  $h_0$  comes from integrating (B.4) along the field line combined with (B.5). For rational surfaces we integrate in the interval  $[0, L]$

$$A(\alpha, L)h_0(\alpha) = \int_0^L s dl - \int_0^L a \exp(-A)W dl \quad (\text{B.10})$$

which also reveals that when  $A(\alpha, L) \neq 0$  equation (B.4) fixes  $h$  on the torus completely.

For irrational flux surfaces, we take the limit  $L \rightarrow \infty$  in condition (B.8) to obtain

$$h_0(\alpha) = h_0(\alpha) \lim_{L \rightarrow \infty} \exp(-A(\alpha, L)) + \lim_{L \rightarrow \infty} W(\alpha, L) \exp(-A(\alpha, L)). \quad (\text{B.11})$$

Thus, the integration constant  $h_0$  can be determined from (B.11) when  $\lim_{L \rightarrow \infty} A(\alpha, L) \neq 0$  and the limit  $\lim_{L \rightarrow \infty} W(\alpha, L) \exp(-A(\alpha, L))$  exists. When it is possible to fix  $h_0$  in irrational surfaces, it is a flux function. A more convenient expression to fix  $h_0$  comes from dividing equation (B.10) by  $\int_0^L dl/B$  and taking the limit  $L \rightarrow \infty$  to obtain

$$\langle Ba \rangle h_0 = \langle Bs \rangle - \langle Ba \exp(-A)W \rangle. \quad (\text{B.12})$$

Note that if  $L_k$  and  $U_k$  are written in the form of (B.4), for both operators, the correspondent function  $a(\alpha, l)$  is proportional to  $\partial \ln B / \partial l$ . This means that for rational surfaces  $A(\alpha, L) = 0$  and when  $\iota$  is irrational  $\lim_{L \rightarrow \infty} A(\alpha, L) = 0$  or equivalently  $\langle Ba \rangle =$

0. Thus, in both cases, there are infinitely many smooth solutions to (B.4) which proves that  $L_k$  and  $U_k$  are not one-to-one. Equivalently, all functions of the form  $h_0 \exp(-A)$  (for the appropriate  $A$ ) belong to the kernel of  $L_k$  and  $U_k$ . Moreover, we obtain conditions on the source  $s(\alpha, l)$ . For rational surfaces,  $W(\alpha, L) = 0$  or equivalently  $\int_0^L s \, dl = \int_0^L a \exp(-A) W \, dl$  and for irrational surfaces  $\lim_{L \rightarrow \infty} W(\alpha, L) = 0$  or equivalently  $\langle Bs \rangle = \langle Ba \exp(-A) W \rangle$ . This means that if we choose a smooth function on the flux surface  $h$  and apply either  $L_k$  or  $U_k$ , the images  $L_k h$  or  $U_k h$  have to satisfy these extra conditions. This proves that  $L_k$  and  $U_k$  are not onto. Therefore, they are clearly not invertible.

Now we will prove that if  $\hat{\nu} \neq 0$ , all the  $D_k$  for  $k \geq 1$  are invertible. For  $\hat{E}_\psi = 0$ ,  $D_k$  is just a multiplication operator and is obviously invertible if  $k \neq 0$ . When  $\hat{E}_\psi \neq 0$  the proof can be done using a similar argument to the one used for  $L_k$  and  $U_k$ , as we can transform  $D_k$  to an equation superficially very similar to (B.4). First, we change from Boozer angles  $(\psi, \theta, \zeta)$  to a different set of magnetic coordinates  $(\tilde{\psi}, \alpha, \varphi)$  using the linear transformation

$$\begin{bmatrix} \psi \\ \theta \\ \zeta \end{bmatrix} = \begin{bmatrix} 1 & 0 & 0 \\ 0 & (1 + \iota\delta)^{-1} & \iota \\ 0 & -\delta(1 + \iota\delta)^{-1} & 1 \end{bmatrix} \begin{bmatrix} \tilde{\psi} \\ \alpha \\ \varphi \end{bmatrix} \quad (\text{B.13})$$

where  $\delta = B_\theta/B_\zeta$ . In these coordinates  $\mathbf{B} = \nabla\tilde{\psi} \times \nabla\alpha = B_{\tilde{\psi}}\nabla\tilde{\psi} + B_\varphi\nabla\varphi$  and

$$\mathbf{B} \times \nabla\tilde{\psi} \cdot \nabla = B^2 \frac{\partial}{\partial\alpha}. \quad (\text{B.14})$$

Thus, in coordinates  $(\alpha, \varphi)$ , the operator  $D_k$  takes the form

$$D_k = -\hat{E}_\psi \frac{B^2}{\langle B^2 \rangle} \frac{\partial}{\partial\alpha} + \hat{\nu} \frac{k(k+1)}{2}. \quad (\text{B.15})$$

Hence, we want to prove that

$$-\hat{E}_\psi \frac{B^2}{\langle B^2 \rangle} \frac{\partial g}{\partial\alpha} + \hat{\nu} \frac{k(k+1)}{2} g = s(\alpha, \varphi) \quad (\text{B.16})$$

has a unique smooth solution for any source  $s$ . The general solution to this equation is

$$g = (g_0(\varphi) + K(\alpha, \varphi)) \exp(A_k(\alpha, \varphi)), \quad (\text{B.17})$$

where  $g_0(\varphi)$  is an integration constant,

$$K(\alpha, \varphi) = -\frac{\langle B^2 \rangle}{E_\psi} \times \int_0^\alpha s(\alpha', \varphi) \exp(-A_k(\alpha', \varphi)) \frac{d\alpha'}{B^2(\alpha', \varphi)} \quad (\text{B.18})$$

and

$$A_k(\alpha, \varphi) = \hat{\nu} \frac{k(k+1)}{2} \frac{\langle B^2 \rangle}{\hat{E}_\psi} \int_0^\alpha \frac{d\alpha''}{B^2(\alpha'', \varphi)}. \quad (\text{B.19})$$

Note from (B.13), that the curves of constant  $\varphi$  are straight lines in the  $(\theta, \zeta)$  plane with slope  $-\delta$ . This means that there are two options if we follow one of these curves: if  $\delta \in \mathbb{Q}$  it closes on itself or if  $\delta \in \mathbb{R} \setminus \mathbb{Q}$  it densely fills the whole flux surface. Applying the same continuity argument used for (B.5) we obtain that in order to fix  $g_0$  either

$$A_k(L_\alpha, \varphi) \neq 0, \quad \text{if } \delta \in \mathbb{Q}, \quad (\text{B.20})$$

or

$$\lim_{\alpha \rightarrow \infty} A_k(\alpha, \varphi) \neq 0, \quad \text{if } \delta \in \mathbb{R} \setminus \mathbb{Q}, \quad (\text{B.21})$$

where  $L_\alpha > 0$  is the arc-length required for the curve of constant  $\varphi$  to close on itself. However, with the exception of  $A_0$  which is identically zero,  $A_k$  is monotonically crescent with  $\alpha$ . For  $k \geq 1$  we can write the integration constant as

$$g_0(\varphi) = -\frac{K(L_\alpha, \varphi)}{1 - \exp(-A_k(L_\alpha, \varphi))}, \quad \text{if } \delta \in \mathbb{Q}, \quad (\text{B.22})$$

or

$$g_0 = -\lim_{\alpha \rightarrow \infty} K(\alpha, \varphi), \quad \text{if } \delta \in \mathbb{R} \setminus \mathbb{Q}. \quad (\text{B.23})$$

Similarly to the constant  $h_0$ , we can obtain equivalent expressions by integrating the differential equation. When  $\delta \in \mathbb{Q}$  applying  $\int_0^{L_\alpha} \text{Eq. (B.16)} \, d\alpha / B^2$  combined with (B.17) gives

$$g_0(\varphi) = \frac{2}{k(k+1)\hat{\nu}} \frac{\int_0^{L_\alpha} s \, d\alpha / B^2}{\int_0^{L_\alpha} \exp(A_k) \, d\alpha / B^2} - \frac{\int_0^{L_\alpha} K \exp(A_k) \, d\alpha / B^2}{\int_0^{L_\alpha} \exp(A_k) \, d\alpha / B^2} \quad (\text{B.24})$$

Note that the annihilator for  $\mathbf{B} \times \nabla\tilde{\psi} \cdot \nabla$  is the flux surface average, i.e.  $\langle \mathbf{B} \times \nabla\tilde{\psi} \cdot \nabla f \rangle = 0$  for any univaluated function on the torus. Using this we can get a more explicit expression for  $g_0$  when  $\delta \in \mathbb{R} \setminus \mathbb{Q}$ . Taking the flux surface average of (B.16) combined with (B.17) gives

$$g_0 = \frac{2}{k(k+1)\hat{\nu}} \frac{\langle s \rangle}{\langle \exp(A_k) \rangle} - \frac{\langle K \exp(A_k) \rangle}{\langle \exp(A_k) \rangle}. \quad (\text{B.25})$$

Hence, for  $k \geq 1$ , we can write the inverse of  $D_k$  as the linear operator

$$D_k^{-1} s = (g_0(\varphi) + K(\alpha, \varphi)) \exp(A_k(\alpha, \varphi)),$$



where  $g_0$  is given by (B.24) or (B.25) and is straightforward to check that  $D_k D_k^{-1} s = D_k^{-1} D_k s = s$ . The operator  $D_0$  is not invertible as it is identically zero for  $\hat{E}_\psi = 0$  and  $A_0 = 0$  for  $\hat{E}_\psi \neq 0$ .

Finally, we will study the invertibility of the operator  $\Delta_k$

$$\Delta_k = D_k - U_k \Delta_{k+1}^{-1} L_{k+1} \quad (\text{B.26})$$

assuming that  $\Delta_{k+1}$  is bounded and invertible. For this, first, we note that in the space of functions of interest (smooth periodic functions on the torus), using a Fourier basis  $\{e^{i(m\theta+nN_p\zeta)}\}_{m,n \in \mathbb{Z}}$ , we can approximate any function  $f(\theta, \zeta) = \sum_{m,n \in \mathbb{Z}} \hat{f}_{mn} e^{i(m\theta+nN_p\zeta)} \in \mathcal{F}$  using an approximant  $\tilde{f}(\theta, \zeta)$

$$\tilde{f}(\theta, \zeta) = \sum_{-N \leq m, n \leq N} \hat{f}_{mn} e^{i(m\theta+nN_p\zeta)} \quad (\text{B.27})$$

truncating the modes with mode number greater than some positive integer  $N$  where

$$\hat{f}_{mn} = \left\langle f, e^{i(m\theta+nN_p\zeta)} \right\rangle_{\mathcal{F}} \left\| e^{i(m\theta+nN_p\zeta)} \right\|_{\mathcal{F}}^{-2} \quad (\text{B.28})$$

are the Fourier modes of  $f$ . Thus, we approximate  $\mathcal{F}$  using a finite dimensional subspace  $\mathcal{F}^N \subset \mathcal{F}$  consisting on all the functions of the form given by equation (B.27).

Hence, as they are bounded operators, we can approximate  $D_k$ ,  $U_k$ ,  $\Delta_{k+1}$  and  $L_{k+1}$  restricted to  $\mathcal{F}^N$  (and therefore  $\Delta_k$ ) in equation (B.26) by operators  $D_k^N$ ,  $U_k^N$ ,  $\Delta_{k+1}^N$  and  $L_{k+1}^N$  that map any  $\tilde{f} \in \mathcal{F}^N$  to the projections of  $D_k \tilde{f}$ ,  $U_k \tilde{f}$ ,  $\Delta_{k+1} \tilde{f}$  and  $L_{k+1} \tilde{f}$  onto  $\mathcal{F}^N$ . The operators  $D_k^N$ ,  $U_k^N$ ,  $\Delta_{k+1}^N$  and  $L_{k+1}^N$  can be exactly represented (in a Fourier basis) by square matrices of size  $\dim \mathcal{F}^N$ . When the operators are invertible, these matrices are invertible aswell. Doing so, we can interpret the matrix representation of  $\Delta_k$  as the Schur complement of the matrix

$$M_k^N = \begin{bmatrix} D_k^N & U_k^N \\ L_{k+1}^N & \Delta_{k+1}^N \end{bmatrix}. \quad (\text{B.29})$$

It is well known from linear algebra that the Schur complement of  $M_k^N$  is invertible when both  $D_k^N$  and  $\Delta_{k+1}^N$  are (which they are). Hence, for  $k \geq 1$ , the matrix representation of  $\Delta_k^N$  can be inverted for any  $N$ , and therefore  $\Delta_k$  is invertible. For  $k = 0$ , it is necessary to substitute one of the rows of  $[D_k^N \ U_k^N]$  by the condition (38) so that  $M_k^N$  is invertible for any  $N$  and as  $\Delta_1^N$  can be inverted, also  $\Delta_0^N$  constructed in this manner for any  $N$ , which implies that  $\Delta_0$  is invertible.

### Appendix C. Fourier collocation method

In this appendix we describe the Fourier collocation (also called pseudospectral) method for discretizing the

angles  $\theta$  and  $\zeta$ . This discretization will be used to obtain the matrices  $\mathbf{L}_k$ ,  $\mathbf{D}_k$  and  $\mathbf{U}_k$ . For convenience, we will use the complex version of the discretization method but for the discretization matrices we will just take their real part as the solutions to (18) are all real. We search for approximate solutions to equation (34) of the form

$$f^{(k)}(\theta, \zeta) = \sum_{n=-N_{\zeta 1}/2}^{N_{\zeta 2}/2-1} \sum_{m=-N_{\theta 1}/2}^{N_{\theta 2}/2-1} \tilde{f}_{mn}^{(k)} e^{i(m\theta+nN_p\zeta)} \quad (\text{C.1})$$

where  $N_{\theta 1} = N_\theta - N_\theta \bmod 2$ ,  $N_{\theta 2} = N_\theta + N_\theta \bmod 2$ ,  $N_{\zeta 1} = N_\zeta - N_\zeta \bmod 2$ ,  $N_{\zeta 2} = N_\zeta + N_\zeta \bmod 2$  for some positive integers  $N_\theta$ ,  $N_\zeta$ . The complex numbers

$$\tilde{f}_{mn}^{(k)} := \left\langle f^{(k)}, e^{i(m\theta+nN_p\zeta)} \right\rangle_{N_\theta N_\zeta} \left\| e^{i(m\theta+nN_p\zeta)} \right\|_{N_\theta N_\zeta}^{-2} \quad (\text{C.2})$$

are the discrete Fourier modes (also called discrete Fourier transform),

$$\langle f, g \rangle_{N_\theta N_\zeta} := \frac{1}{N_\theta N_\zeta} \sum_{j'=0}^{N_\zeta-1} \sum_{i'=0}^{N_\theta-1} f(\theta_{i'}, \zeta_{j'}) \overline{g(\theta_{i'}, \zeta_{j'})}, \quad (\text{C.3})$$

is the discrete inner product associated to the equispaced grid points (49), (50),  $\|f\|_{N_\theta N_\zeta} := \sqrt{\langle f, f \rangle_{N_\theta N_\zeta}}$  its induced norm and  $\bar{z}$  denotes the complex conjugate of  $z$ . We denote by  $\mathcal{F}^{N_\theta N_\zeta}$  to the finite dimensional vector space (of dimension  $N_\theta N_\zeta$ ) comprising all the functions that can be written in the form of expansion (C.1).

The set of functions  $\{e^{i(m\theta+nN_p\zeta)}\} \subset \mathcal{F}^{N_\theta N_\zeta}$  forms an orthogonal basis for  $\mathcal{F}^{N_\theta N_\zeta}$  equipped with the discrete inner product (C.3). Namely,

$$\left\langle e^{i(m\theta+nN_p\zeta)}, e^{i(m'\theta+n'N_p\zeta)} \right\rangle_{N_\theta N_\zeta} \propto \delta_{mm'} \delta_{nn'} \quad (\text{C.4})$$

for  $-N_{\theta 1}/2 \leq m \leq N_{\theta 2}/2$  and  $-N_{\zeta 1}/2 \leq n \leq N_{\zeta 2}/2$ . Thus, for functions lying in  $\mathcal{F}^{N_\theta N_\zeta}$ , discrete expansions such as (C.1) coincide with their (finite) Fourier series. The discrete Fourier modes (C.2) are chosen so that the expansion (C.1) interpolates  $f^{(k)}$  at grid points. Thus, there is a vector space isomorphism between the space of discrete Fourier modes and  $f^{(k)}$  evaluated at the equispaced grid.

Combining equations (C.1), (C.2) and (C.3) we can write our Fourier interpolant as

$$\begin{aligned} f^{(k)}(\theta, \zeta) &= \mathbf{I}(\theta, \zeta) \cdot \mathbf{f}^{(k)} \\ &= \sum_{j'=0}^{N_\zeta-1} \sum_{i'=0}^{N_\theta-1} I_{i'j'}(\theta, \zeta) f^{(k)}(\theta_{i'}, \zeta_{j'}), \end{aligned} \quad (\text{C.5})$$

where  $\mathbf{f}^{(k)} \in \mathbb{R}^{N_{fs}}$  is the state vector containing  $f^{(k)}(\theta_{i'}, \zeta_{j'})$ . The entries of the vector  $\mathbf{I}(\theta, \zeta)$  are the functions  $I_{i'j'}(\theta, \zeta)$  given by,

$$I_{i'j'}(\theta, \zeta) = I_{i'}^\theta(\theta) I_{j'}^\zeta(\zeta), \quad (C.6)$$

$$I_{i'}^\theta(\theta) = \frac{1}{N_\theta} \sum_{m=-N_{\theta 1}/2}^{N_{\theta 2}/2-1} e^{im(\theta-\theta_{i'})}, \quad (C.7)$$

$$I_{j'}^\zeta(\zeta) = \frac{1}{N_\zeta} \sum_{n=-N_{\zeta 1}/2}^{N_{\zeta 2}/2-1} e^{N_p \text{in}(\zeta-\zeta_{j'})}. \quad (C.8)$$

Note that the interpolant is the only function in  $\mathcal{F}^{N_\theta N_\zeta}$  which interpolates the data at the grid points, as  $I_{i'}^\theta(\theta_i) = \delta_{ii'}$  and  $I_{j'}^\zeta(\zeta_j) = \delta_{jj'}$ .

Of course, our approximation (C.5) cannot (in general) be a solution to (34) at all points  $(\theta, \zeta) \in [0, 2\pi) \times [0, 2\pi/N_p)$ . Instead, we will force that the interpolant (C.5) solves equation (34) exactly at the equispaced grid points. Thanks to the vector space isomorphism (C.2) between  $\mathbf{f}^{(k)}$  and the discrete modes  $\tilde{f}_{mn}^{(k)}$  this is equivalent to match the discrete Fourier modes of the left and right-hand-sides of equation (34).

Inserting the interpolant (C.5) in the left-hand side of equation (34) and evaluating the result at grid points gives

$$\left( L_k f^{(k-1)} + D_k f^{(k)} + U_k f^{(k)} \right) \Big|_{(\theta_i, \zeta_j)} = \quad (C.9)$$

$$\left( L_k \mathbf{I} \cdot \mathbf{f}^{(k-1)} + D_k \mathbf{I} \cdot \mathbf{f}^{(k)} + U_k \mathbf{I} \cdot \mathbf{f}^{(k+1)} \right) \Big|_{(\theta_i, \zeta_j)}.$$

Here,  $L_k \mathbf{I}(\theta_i, \zeta_j)$ ,  $D_k \mathbf{I}(\theta_i, \zeta_j)$  and  $U_k \mathbf{I}(\theta_i, \zeta_j)$  are respectively the rows of  $\mathbf{L}_k$ ,  $\mathbf{D}_k$  and  $\mathbf{U}_k$  associated to the grid point  $(\theta_i, \zeta_j)$ . We can relate them to the actual positions they will occupy in the matrices choosing an ordination of rows and columns. If we use the ordination that relates respectively the row  $i_r$  and column  $i_c$  to the grid points  $(\theta_i, \zeta_j)$  and  $(\theta_{i'}, \zeta_{j'})$  as

$$i_r = 1 + i + j N_\theta, \quad (C.10)$$

$$i_c = 1 + i' + j' N_\theta, \quad (C.11)$$

for  $i, i' = 0, 1, \dots, N_\theta - 1$  and  $j, j' = 0, 1, \dots, N_\zeta - 1$ . With this ordination, we define the elements of the row  $i_r$  and column  $i_c$  given by (C.10) and (C.11) of the matrices  $\mathbf{L}_k$ ,  $\mathbf{D}_k$  and  $\mathbf{U}_k$  to be

$$(\mathbf{L}_k)_{i_r i_c} = L_k I_{i'j'}(\theta_i, \zeta_j), \quad (C.12)$$

$$(\mathbf{D}_k)_{i_r i_c} = D_k I_{i'j'}(\theta_i, \zeta_j), \quad (C.13)$$

$$(\mathbf{U}_k)_{i_r i_c} = U_k I_{i'j'}(\theta_i, \zeta_j). \quad (C.14)$$

Explicitly,

$$L_k I_{i'j'} \Big|_{(\theta_i, \zeta_j)} = \frac{k}{2k-1} \left( \mathbf{b} \cdot \nabla I_{i'j'} \Big|_{(\theta_i, \zeta_j)} + \frac{k-1}{2} \mathbf{b} \cdot \nabla \ln B \Big|_{(\theta_i, \zeta_j)} \delta_{ii'} \delta_{jj'} \right), \quad (C.15)$$

$$D_k I_{i'j'} \Big|_{(\theta_i, \zeta_j)} = \frac{\hat{E}_\psi}{\langle B^2 \rangle} \mathbf{B} \times \nabla \psi \cdot \nabla I_{i'j'} \Big|_{(\theta_i, \zeta_j)} + \frac{k(k+1)}{2} \hat{\nu} \delta_{ii'} \delta_{jj'}, \quad (C.16)$$

$$U_k I_{i'j'} \Big|_{(\theta_i, \zeta_j)} = \frac{k+1}{2k+3} \left( \mathbf{b} \cdot \nabla I_{i'j'} \Big|_{(\theta_i, \zeta_j)} + \frac{k+2}{2} \mathbf{b} \cdot \nabla \ln B \Big|_{(\theta_i, \zeta_j)} \delta_{ii'} \delta_{jj'} \right), \quad (C.17)$$

where we have used expressions (31) and (32) to write

$$\mathbf{b} \cdot \nabla I_{i'j'} \Big|_{(\theta_i, \zeta_j)} = \frac{B}{B_\zeta + \iota B_\theta} \Big|_{(\theta_i, \zeta_j)} \times \left( \iota \delta_{jj'} \frac{dI_{i'}^\theta}{d\theta} \Big|_{\theta_i} - \delta_{ii'} \frac{dI_{j'}^\zeta}{d\zeta} \Big|_{\zeta_j} \right) \quad (C.18)$$

$$\mathbf{B} \times \nabla \psi \cdot \nabla I_{i'j'} \Big|_{(\theta_i, \zeta_j)} = \frac{B^2}{B_\zeta + \iota B_\theta} \Big|_{(\theta_i, \zeta_j)} \times \left( B_\zeta \delta_{jj'} \frac{dI_{i'}^\theta}{d\theta} \Big|_{\theta_i} - B_\theta \delta_{ii'} \frac{dI_{j'}^\zeta}{d\zeta} \Big|_{\zeta_j} \right) \quad (C.19)$$

We remark in first place that, for  $k = 0$ , the rows of  $\mathbf{D}_0$  and  $\mathbf{U}_0$  associated to the grid point  $(\theta_0, \zeta_0) = (0, 0)$ , are replaced by equation (38). Finally, each state vector  $\mathbf{f}^{(k)}$  for the Fourier interpolants contains the images  $f^{(k)}(\theta_{i'}, \zeta_{j'})$  at the grid points, ordered according to (C.11).

#### Appendix D. Convergence of monoenergetic coefficients calculated by DKES

The code DKES gives an approximation to the monoenergetic geometric coefficients as a semisum of two quantities  $\hat{D}_{ij}^-$  and  $\hat{D}_{ij}^{++}$  by solving a variational principle [29]. For each coefficient, the output of DKES consists on two columns containing  $\hat{D}_{ij}^\mp K_{ij}$ , where  $K_{ij}$

+ The columns

are the normalization factors

$$K_{ij} := \left( \frac{d\psi}{dr} \right)^{-2}, \quad i, j \in \{1, 2\}, \quad (\text{D.1})$$

$$K_{i3} := \left( \frac{d\psi}{dr} \right)^{-1}, \quad i \in \{1, 2\}, \quad (\text{D.2})$$

$$K_{3j} := \left( \frac{d\psi}{dr} \right)^{-1}, \quad j \in \{1, 2\}, \quad (\text{D.3})$$

$$K_{33} := 1, \quad (\text{D.4})$$

where  $B_{00} = N_p (2\pi)^{-2} \oint \oint B \, d\theta \, d\zeta$  is the  $(0, 0)$  Fourier mode of  $B$ .

There is still a nuance left for the parallel conductivity coefficient: the code **DKES** computes this coefficient measured with respect to the one obtained by solving the Spitzer problem

$$-\hat{\nu} \mathcal{L} f_{\text{Sp}} = s_3. \quad (\text{D.5})$$

Using (A.1) is immediate to obtain the 1-th Legendre mode of  $f_{\text{Sp}}$

$$f_{\text{Sp}}^{(1)} = \frac{1}{\hat{\nu}} \frac{B}{B_0} \quad (\text{D.6})$$

and using (47) we obtain its associated  $\hat{D}_{33}$  coefficient

$$\hat{D}_{33, \text{Sp}} = \frac{2}{3\hat{\nu}} \left\langle \frac{B^2}{B_0^2} \right\rangle. \quad (\text{D.7})$$

Thus, the output columns of **DKES** for the parallel conductivity coefficient have to be compared against the deviation  $(\hat{D}_{33} - \hat{D}_{33, \text{Sp}})$ .

In this Appendix we plot how the monoenergetic coefficients calculated by **DKES** converge. From the output of **DKES**, the two columns  $\hat{D}_{ij}^\pm$  satisfy  $\hat{D}_{ij}^- \geq \hat{D}_{ij}^+$  and allow to compute bounds for  $\hat{D}_{ij}$

$$\frac{\hat{D}_{ij}^- + \hat{D}_{ij}^+}{2} - \Delta_{ij} \leq \hat{D}_{ij} \leq \frac{\hat{D}_{ij}^- + \hat{D}_{ij}^+}{2} + \Delta_{ij} \quad (\text{D.8})$$

and  $\Delta_{ij} = \frac{1}{2} \sqrt{(\hat{D}_{ii}^- - \hat{D}_{ii}^+)(\hat{D}_{jj}^- - \hat{D}_{jj}^+)}.$

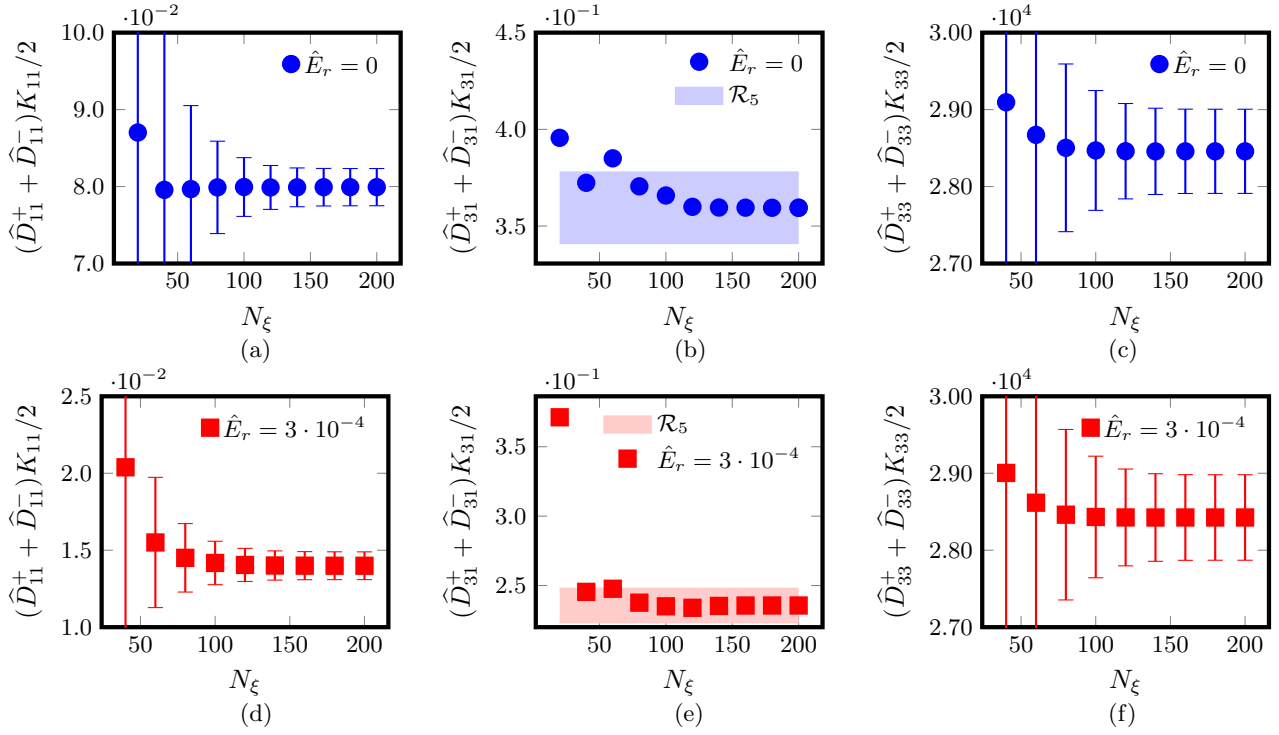


Figure D1: Convergence of monoenergetic coefficients calculated with DKES for W7X-EIM at the surface labelled by  $\psi/\psi_{\text{lcf}} = 0.200$ .  $\hat{E}_r$  in  $\text{kV} \cdot \text{s}/\text{m}^2$ .

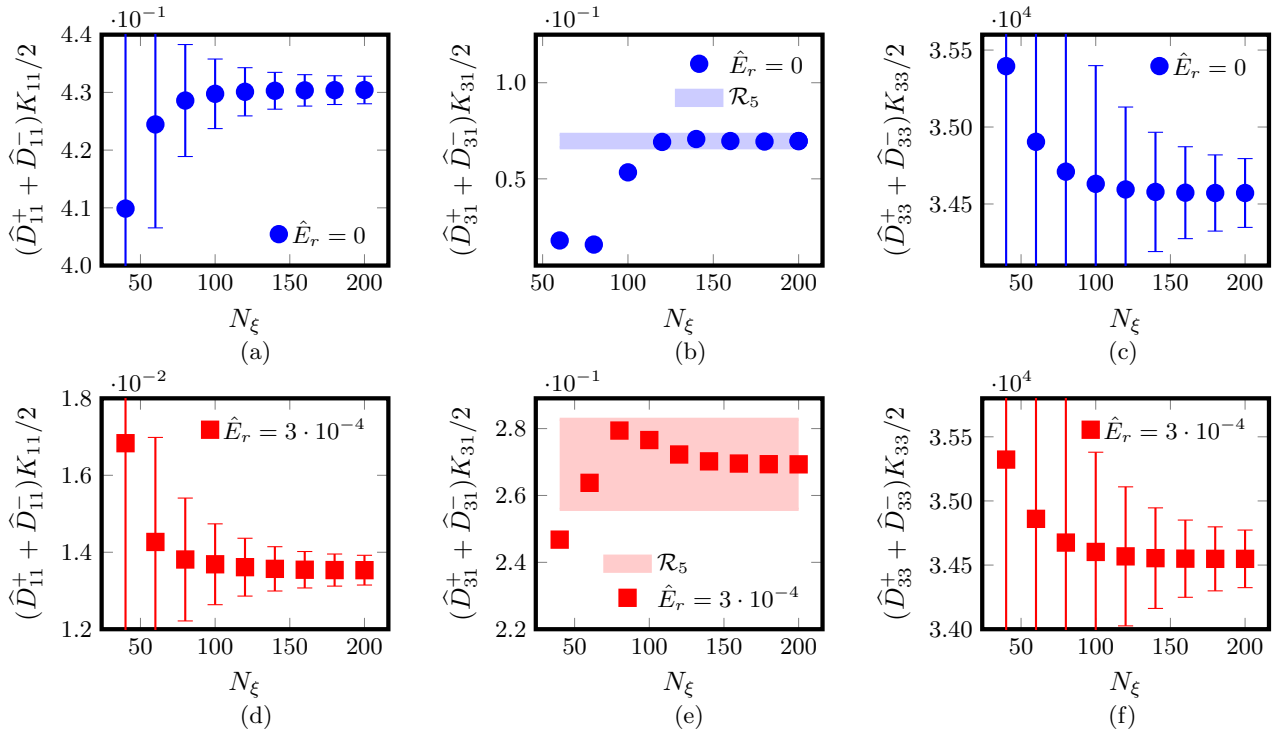


Figure D2: Convergence of monoenergetic coefficients calculated with DKES for W7X-KJM at the surface labelled by  $\psi/\psi_{\text{lcf}} = 0.204$ .  $\hat{E}_r$  in  $\text{kV} \cdot \text{s}/\text{m}^2$ .

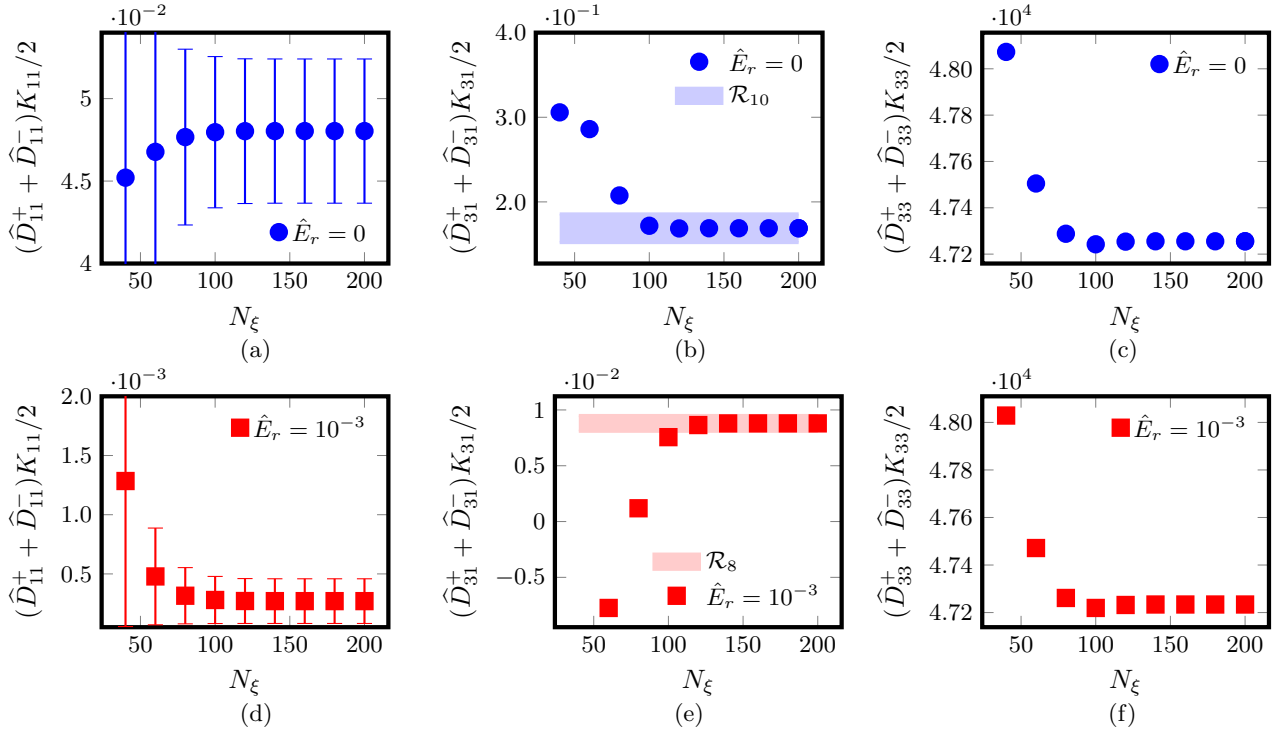


Figure D3: Convergence of monoenergetic coefficients calculated with DKES for CIEMAT-QI at the surface labelled by  $\psi/\psi_{\text{lcs}} = 0.250$ .  $\hat{E}_r$  in  $\text{kV} \cdot \text{s/m}^2$ .

## Acknowledgements

## References

- [1] John R. Cary and Svetlana G. Shasharina. Omnigenity and quasihelicity in helical plasma confinement systems. *Physics of Plasmas*, 4:3323–3333, 1997.
- [2] P Helander and J Nührenberg. Bootstrap current and neoclassical transport in quasi-isodynamic stellarators. *Plasma Physics and Controlled Fusion*, 51(5):055004, feb 2009.
- [3] P. Helander, J. Geiger, and H. Maaßberg. On the bootstrap current in stellarators and tokamaks. *Physics of Plasmas*, 18(9), 09 2011. 092505.
- [4] C. D. Beidler, H. M. Smith, A. Alonso, T. Andreeva, J. Baldzuhn, M. N. A. Beurskens, M. Borchardt, S. A. Bozhnikov, K. J. Brunner, H. Damm, M. Drevlak, O. P. Ford, G. Fuchert, J. Geiger, P. Helander, U. Hergenhan, M. Hirsch, U. Höfel, Ye. O. Kazakov, R. Kleiber, M. Krychowiak, S. Kwak, A. Langenberg, H. P. Laqua, U. Neuner, N. A. Pablant, E. Pasch, A. Pavone, T. S. Pedersen, K. Rahbarnia, J. Schilling, E. R. Scott, T. Stange, J. Svensson, H. Thomsen, Y. Turkin, F. Warmer, R. C. Wolf, D. Zhang, I. Abramovic, S. Äkäslompolo, J. Alcúsn, P. Aleynikov, K. Aleynikova, A. Ali, G. Anda, E. Ascasibar, J. P. Böhner, S. G. Baek, M. Balden, M. Banduch, T. Barbui, W. Behr, A. Benndorf, C. Biedermann, W. Biel, B. Blackwell, E. Blanco, M. Blatzheim, S. Ballinger, T. Bluhm, D. Böckenhoff, B. Böswirth, L.-G. Böttger, V. Borsuk, J. Boscary, H.-S. Bosch, R. Brakel, H. Brand, C. Brandt, T. Bräuer, H. Braune, S. Brezinsek, K.-J. Brunner, R. Burhenn, R. Bussiahn, B. Buttenschön, V. Bykov, J. Cai, I. Calvo, B. Cannas, A. Cappa, A. Carls, L. Carraro, B. Carvalho, F. Castejon, A. Charl,

N. Chaudhary, D. Chauvin, F. Chernyshev, M. Cianciosa, R. Citarella, G. Claps, J. Coenen, M. Cole, M. J. Cole, F. Cordella, G. Cseh, A. Czarnecka, K. Czerski, M. Czerwinski, G. Czymek, A. da Molin, A. da Silva, A. de la Pena, S. Degenkolbe, C. P. Dhard, M. Dibon, A. Dinklage, T. Dittmar, P. Drewelow, P. Drews, F. Durodie, E. Edlund, F. Effenberg, G. Ehrke, S. Elgeti, M. Endler, D. Ennis, H. Esteban, T. Estrada, J. Fellingner, Y. Feng, E. Flom, H. Fernandes, W. H. Fietz, W. Figacz, J. Fontdecaba, T. Fornal, H. Frerichs, A. Freund, T. Funaba, A. Galkowski, G. Gantenbein, Y. Gao, J. García Regaña, D. Gates, B. Geiger, V. Giannela, A. Gogoleva, B. Goncalves, A. Gorlaev, D. Gradic, M. Grahl, J. Green, H. Greuner, A. Grosman, H. Grote, M. Gruca, O. Grulke, C. Guerard, P. Hacker, X. Han, J. H. Harris, D. Hartmann, D. Hathiramani, B. Hein, B. Heinemann, S. Henneberg, M. Henkel, J. Hernandez Sanchez, C. Hidalgo, K. P. Hollfeld, A. Hölting, D. Höschen, M. Houry, J. Howard, X. Huang, Z. Huang, M. Hubeny, M. Huber, H. Hunger, K. Ida, T. Ilkei, S. Illy, B. Israeli, S. Jablonski, M. Jakubowski, J. Jelonnek, H. Jenzsch, T. Jesche, M. Jia, P. Junghanns, J. Kacmarczyk, J.-P. Kallmeyer, U. Kamionka, H. Kasahara, W. Kasperek, N. Kenmochi, C. Killer, A. Kirschner, T. Klinger, J. Knauer, M. Knaup, A. Knieps, T. Kobarg, G. Kocsis, F. Köchl, Y. Kolesnichenko, A. Könies, R. König, P. Kornejew, J.-P. Koschinsky, F. Köster, M. Krämer, R. Krampitz, A. Krämer-Flecken, N. Krawczyk, T. Kremeyer, J. Krom, I. Ksiazek, M. Kubkowska, G. Kühner, T. Kurki-Suonio, P. A. Kurz, M. Landreman, P. Lang, R. Lang, S. Langish, H. Laqua, R. Laube, S. Lazerson, C. Lechte, M. Lennartz, W. Leonhardt, C. Li, Y. Li, Y. Liang, C. Linsmeier, S. Liu, J.-F. Lobsien, D. Loesser, J. Loizu Cisquella, J. Lore, A. Lorenz, M. Losert, A. Lücke, A. Lumsdaine, V. Lut-

- senko, H. Maaßberg, O. Marchuk, J. H. Matthew, S. Marsen, M. Marushchenko, S. Masuzaki, D. Maurer, M. Mayer, K. McCarthy, P. McNeely, A. Meier, D. Mellein, B. Mendelevitch, P. Mertens, D. Mikkelsen, A. Mishchenko, B. Missal, J. Mittelstaedt, T. Mizuuchi, A. Mollen, V. Moncada, T. Mönnich, T. Morisaki, D. Moseev, S. Murakami, G. Náfrádi, M. Nagel, D. Naujoks, H. Neilson, R. Neu, O. Neubauer, T. Ngo, D. Nicolai, S. K. Nielsen, H. Niemann, T. Nishizawa, R. Nocentini, C. Nührenberg, J. Nührenberg, S. Obermayer, G. Offermanns, K. Ogawa, J. Ölmanns, J. Ongena, J. W. Oosterbeek, G. Orozco, M. Otte, L. Pacios Rodriguez, N. Panadero, N. Panadero Alvarez, D. Papenfuß, S. Paqay, E. Pawelec, G. Pelka, V. Perseo, and the W7-X Team. Demonstration of reduced neoclassical energy transport in wendelstein 7-x. *Nature*, 596(7871):221–226, Aug 2021.
- [5] A. Dinklage, C. D. Beidler, P. Helander, G. Fuchert, H. Maaßberg, K. Rahbarnia, T. Sunn Pedersen, Y. Turkin, R. C. Wolf, A. Alonso, T. Andreeva, B. Blackwell, S. Bozhnikov, B. Buttenschön, A. Czarnecka, F. Effenberg, Y. Feng, J. Geiger, M. Hirsch, U. Höfel, M. Jakubowski, T. Klinger, J. Knauer, G. Kocsis, A. Krämer-Flecken, M. Kubkowska, A. Langenberg, H. P. Laqua, N. Marushchenko, A. Mollén, U. Neuner, H. Niemann, E. Pasch, N. Pablant, L. Rudischhauser, H. M. Smith, O. Schmitz, T. Stange, T. Szepesi, G. Weir, T. Windisch, G. A. Wurden, D. Zhang, I. Abramovic, S. Äkäslompolo, A. Ali, J. Alcuson Belloso, P. Aleynikov, K. Aleynikova, R. Alzbutas, G. Anda, E. Ascasibar, J. Assmann, S.-G. Baek, J. Baldzuhn, M. Banduch, T. Barbui, M. Barlak, K. Baumann, W. Behr, C. Beidler, A. Benndorf, O. Bertuch, M. Beurskens, C. Biedermann, W. Biel, D. Birus, E. Blanco, M. Blatzheim, T. Bluhm, D. Böckenhoff, P. Bolgert, M. Borchardt, V. Borsuk, J. Boscary, H.-S. Bosch, L.-G. Böttger, R. Brakel, H. Brand, Ch. Brandt, T. Bräuer, H. Braune, S. Brezinsek, K.-J. Brunner, B. Brünner, R. Burhenn, R. Bussiahn, V. Bykov, Y. Cai, I. Calvo, B. Cannas, A. Cappa, A. Card, A. Carls, L. Carraro, B. Carvalho, F. Castejon, A. Charl, F. Chernyshev, M. Cianciosa, R. Citarella, L. Ciupiński, G. Claps, M. J. Cole, F. Cordella, G. Cseh, A. Czermak, K. Czerski, M. Czerwinski, G. Czymek, A. da Molin, A. da Silva, G. Dammertz, A. de la Pena, S. Degenkolbe, P. Denner, T. Dittmar, C. P. Dhard, M. Dostal, M. Drevlak, P. Drewelow, Ph. Drews, A. Dudek, G. Dundulis, F. Durodie, P. van Eeten, G. Ehrke, M. Endler, D. Ennis, E. Erckmann, H. Esteban, T. Estrada, N. Fahrenkamp, J.-H. Feist, J. Fellingner, H. Fernandes, W. H. Fietz, W. Figacz, J. Fontdecaba, O. Ford, T. Fornal, H. Frerichs, A. Freund, M. Führer, P. Funaba, A. Galkowski, G. Gantenbein, Y. Gao, J. García Regaña, M. Garcia-Munoz, D. Gates, G. Gawlik, B. Geiger, V. Giannella, N. Gierse, A. Gogoleva, B. Goncalves, A. Gorlaev, D. Gradic, M. Grahl, J. Green, A. Grosman, H. Grote, M. Gruca, O. Grulke, C. Guerard, P. Hacker, L. Haiduk, K. Hammond, X. Han, F. Harberts, J. H. Harris, H.-J. Hartfuß, D. Hartmann, D. Hathiramani, B. Hein, B. Heinemann, P. Heitzenroeder, S. Henneberg, C. Hennig, J. Hernandez Sanchez, C. Hidalgo, H. Hölbe, K. P. Hollfeld, A. Hölting, D. Höschen, M. Houry, J. Howard, X. Huang, M. Huber, V. Huber, H. Hunger, K. Ida, T. Ilkei, S. Illy, B. Israeli, A. Ivanov, S. Jablonski, J. Jagielski, J. Jelonek, H. Jenzsch, P. Junghans, J. Kacmarczyk, T. Kalitka, J.-P. Kallmeyer, U. Kamionka, R. Karalevichius, H. Kasahara, W. Kasperek, Y. Kazakov, N. Kenmochi, M. Keunecke, A. Khilchenko, C. Killer, D. Kinna, R. Kleiber, M. Knaup, A. Knieps, Th. Kobarg, F. Köchl, Y. Kolesnichenko, A. Könies, M. Köppen, J. Koshurin, R. Koslowski, R. König, F. Köster, P. Kornejew, R. Koziol, M. Krämer, R. Krampitz, P. Kraszewski, N. Krawczyk, T. Kremeyer, Th. Krings, J. Krom, M. Krychowiak, G. Krzesinski, I. Ksiazek, G. Kühner, T. Kurki-Suonio, S. Kwak, M. Landreman, R. Lang, S. Langish, H. Laqua, H. P. Laqua, R. Laube, S. Lazerson, C. Lechte, M. Lennartz, W. Leonhardt, L. Lewerentz, Y. Liang, Ch. Linsmeier, S. Liu, J.-F. Lobsien, D. Loesser, J. Loizu Cisque, J. Lore, A. Lorenz, M. Losert, L. Lubyako, A. Lücke, A. Lumsdaine, V. Lutsenko, J. Maisano-Brown, O. Marchuk, M. Mardenfeld, P. Marek, S. Marsen, M. Marushchenko, S. Masuzaki, D. Maurer, K. McCarthy, P. McNeely, A. Meier, , and the W7-X Team. Magnetic configuration effects on the wendelstein 7-x stellarator. *Nature Physics*, 14(8):855–860, Aug 2018.
- [6] E. Sánchez, J.L. Velasco, I. Calvo, and S. Mulas. A quasi-isodynamic configuration with good confinement of fast ions at low plasma beta. *Nuclear Fusion*, 63(6):066037, may 2023.
- [7] J. L. Velasco, I. Calvo, E. Sánchez, and F. I. Parra. Robust stellarator optimization via flat mirror magnetic fields, 2023.
- [8] R. Jorge, G.G. Plunk, M. Drevlak, M. Landreman, J.-F. Lobsien, K. Camacho Mata, and P. Helander. A single-field-period quasi-isodynamic stellarator. *Journal of Plasma Physics*, 88(5):175880504, 2022.
- [9] Katia Camacho Mata, Gabriel G. Plunk, and Rogerio Jorge. Direct construction of stellarator-symmetric quasi-isodynamic magnetic configurations. *Journal of Plasma Physics*, 88(5):905880503, 2022.
- [10] Alan Goodman, Katia Camacho Mata, Sophia A Henneberg, Rogerio Jorge, Matt Landreman, Gabriel Plunk, Hakan Smith, Ralf Mackenbach, and Per Helander. Constructing precisely quasi-isodynamic magnetic fields, 2022.
- [11] A. Pytte and Allen H. Boozer. Neoclassical transport in helically symmetric plasmas. *The Physics of Fluids*, 24(1):88–92, 01 1981.
- [12] Allen H. Boozer. Transport and isomorphic equilibria. *The Physics of Fluids*, 26(2):496–499, 02 1983.
- [13] Matt Landreman and Elizabeth Paul. Magnetic fields with precise quasisymmetry for plasma confinement. *Phys. Rev. Lett.*, 128:035001, Jan 2022.
- [14] Per Helander. Theory of plasma confinement in non-axisymmetric magnetic fields. *Reports on Progress in Physics*, 77(8):087001, jul 2014.
- [15] F. Simon B. Anderson, Abdulgader F. Almagri, David T. Anderson, Peter G. Matthews, Joseph N. Talmadge, and J. Leon Shohet. The helically symmetric experiment, (hsx) goals, design and status. *Fusion Technology*, 27(3T):273–277, 1995.
- [16] M C Zarnstorff, L A Berry, A Brooks, E Fredrickson, G-Y Fu, S Hirshman, S Hudson, L-P Ku, E Lazarus, D Mikkelsen, D Monticello, G H Neilson, N Pomphrey, A Reiman, D Spong, D Strickler, A Boozer, W A Cooper, R Goldston, R Hatcher, M Isaev, C Kessel, J Lewandowski, J F Lyon, P Merkel, H Mynick, B E Nelson, C Nuehrenberg, M Redi, W Reiersen, P Rutherford, R Sanchez, J Schmidt, and R B White. Physics of the compact advanced stellarator ncxs. *Plasma Physics and Controlled Fusion*, 43(12A):A237, nov 2001.
- [17] Viktor V. Nemov, Sergei V. Kasilov, Winfried Kernbichler, and Martin F. Heyn. Evaluation of  $1/\nu$  neoclassical transport in stellarators. *Physics of Plasmas*, 6:4622–4632, 1999.
- [18] K. C. Shaing and J. D. Callen. Neoclassical flows and transport in nonaxisymmetric toroidal plasmas. *The Physics of Fluids*, 26(11):3315–3326, 11 1983.

- [19] N. Nakajima, M. Okamoto, J. Todoroki, Y. Nakamura, and M. Wakatani. Optimization of bootstrap current in a large helical system with  $L = 2$ , August 1988.
- [20] P. Helander, F. I. Parra, and S. L. Newton. Stellarator bootstrap current and plasma flow velocity at low collisionality. *Journal of Plasma Physics*, 83(2):905830206, 2017.
- [21] M. Landreman, S. Buller, and M. Drevlak. Optimization of quasi-symmetric stellarators with self-consistent bootstrap current and energetic particle confinement. *Physics of Plasmas*, 29(8), 08 2022. 082501.
- [22] Iván Calvo, Felix I Parra, José Luis Velasco, and J Arturo Alonso. The effect of tangential drifts on neoclassical transport in stellarators close to omnigenity. *Plasma Physics and Controlled Fusion*, 59(5):055014, mar 2017.
- [23] Vincent d’Herbemont, Felix I. Parra, Iván Calvo, and José Luis Velasco. Finite orbit width effects in large aspect ratio stellarators. *Journal of Plasma Physics*, 88(5):905880507, 2022.
- [24] J.L. Velasco, I. Calvo, F.I. Parra, and J.M. García-Regaña. Knosos: A fast orbit-averaging neoclassical code for stellarator geometry. *Journal of Computational Physics*, 418:109512, 2020.
- [25] J.L. Velasco, I. Calvo, F.I. Parra, V. d’Herbemont, H.M. Smith, D. Carralero, T. Estrada, and the W7-X Team. Fast simulations for large aspect ratio stellarators with the neoclassical code knosos. *Nuclear Fusion*, 61(11):116013, sep 2021.
- [26] Samuel Lazerson, John Schmitt, Caoxiang Zhu, Joshua Breslau, All STELLOPT Developers, and USDOE Office of Science. Stellopt, version 2.7.5, 5 2020.
- [27] A. Bañón Navarro, A. Di Siena, J.L. Velasco, F. Wilms, G. Merlo, T. Windisch, L.L. LoDestro, J.B. Parker, and F. Jenko. First-principles based plasma profile predictions for optimized stellarators. *Nuclear Fusion*, 63(5):054003, mar 2023.
- [28] M. Barnes, I. G. Abel, W. Dorland, T. Görler, G. W. Hammett, and F. Jenko. Direct multiscale coupling of a transport code to gyrokinetic turbulence codesa). *Physics of Plasmas*, 17(5):056109, 04 2010.
- [29] W. I. van Rij and S. P. Hirshman. Variational bounds for transport coefficients in three-dimensional toroidal plasmas. *Physics of Fluids B: Plasma Physics*, 1(3):563–569, 1989.
- [30] M. Landreman, H. M. Smith, A. Mollén, and P. Helander. Comparison of particle trajectories and collision operators for collisional transport in nonaxisymmetric plasmas. *Physics of Plasmas*, 21(4):042503, 2014.
- [31] P Helander and DJ Sigmar. *Collisional transport in magnetized plasmas*. Cambridge university press, 2005.
- [32] S. P. Hirshman, K. C. Shaing, W. I. van Rij, C. O. Beasley, and E. C. Crume. Plasma transport coefficients for nonsymmetric toroidal confinement systems. *The Physics of Fluids*, 29(9):2951–2959, 1986.
- [33] C.D. Beidler, K. Allmaier, M.Yu. Isaev, S.V. Kasilov, W. Kernbichler, G.O. Leitold, H. Maaßberg, D.R. Mikkelsen, S. Murakami, M. Schmidt, D.A. Spong, V. Tribaldos, and A. Wakasa. Benchmarking of the mono-energetic transport coefficients—results from the international collaboration on neoclassical transport in stellarators (icnts). *Nuclear Fusion*, 51(7):076001, jun 2011.
- [34] Matt Landreman. The monoenergetic approximation in stellarator neoclassical calculations. *Plasma Physics and Controlled Fusion*, 53(8):082003, jun 2011.
- [35] Lloyd N. Trefethen and J. A. C. Weideman. The exponentially convergent trapezoidal rule. *SIAM Review*, 56(3):385–458, 2014.
- [36] E. Anderson, Z. Bai, C. Bischof, S. Blackford, J. Demmel, J. Dongarra, J. Du Croz, A. Greenbaum, S. Hammarling, A. McKenney, and D. Sorensen. *LAPACK Users’ Guide*. Society for Industrial and Applied Mathematics, Philadelphia, PA, third edition, 1999.
- [37] J. L. Tennyson, John R. Cary, and D. F. Escande. Change of the adiabatic invariant due to separatrix crossing. *Phys. Rev. Lett.*, 56:2117–2120, May 1986.
- [38] H. Sugama and W. Horton. Entropy production and Onsager symmetry in neoclassical transport processes of toroidal plasmas. *Physics of Plasmas*, 3(1):304–322, 01 1996.